ISPRS Journal of Photogrammetry and Remote Sensing 192 (2022) 99–114

Contents lists available at ScienceDirect

ISPRS Journal of Photogrammetry and Remote Sensing

journal homepage: www.elsevier.com/locate/isprsjprs

Assessment of PRISMA water reflectance using autonomous hyperspectral radiometry

Federica Braga [a,*], Alice Fabbretto [b,c], Quinten Vanhellemont [d], Mariano Bresciani [b], Claudia Giardino [b], Gian Marco Scarpa [a], Giorgia Manfè [a], Javier Alonso Concha [e,f], Vittorio Ernesto Brando [g]

[a] Consiglio Nazionale delle Ricerche, Istituto di Scienze Marine (CNR-ISMAR), Venice, Italy
[b] Consiglio Nazionale delle Ricerche, Istituto per il Rilevamento Elettromagnetico dell'Ambiente (CNR-IREA), Milan, Italy
[c] Tartu Observatory, University of Tartu, Tartu County, Estonia
[d] Royal Belgian Institute of Natural Sciences, Operational Directorate Natural Environments, Brussels, Belgium
[e] European Space Agency (ESA-ESRIN), Frascati, Italy
[f] Serco S.p.A, Frascati, Italy
[g] Consiglio Nazionale delle Ricerche, Istituto di Scienze Marine (CNR-ISMAR), Rome, Italy

ARTICLE INFO

Keywords:
Imaging spectroscopy
Autonomous hyperspectral radiometer systems
Coastal and inland waters
Atmospheric correction
PRISMA mission

ABSTRACT

Hyperspectral remote sensing reflectance (Rrs) derived from PRISMA in the visible and infrared range was evaluated for two inland and coastal water sites using above-water *in situ* reflectance measurements from autonomous hyper- and multispectral radiometer systems. We compared the Level 2D (L2D) surface reflectance, a standard product distributed by the Italian Space Agency (ASI), as well as outputs from ACOLITE/DSF, now adapted for processing of PRISMA imagery. Near-coincident Sentinel-3 OLCI (S3/OLCI) observations were also compared as it is a frequent data source for inland and coastal water remote sensing applications, with a strong calibration and validation record. *In situ* measurements from two optically diverse sites in Italy, equipped with fixed autonomous hyperspectral radiometer systems, were used: the REmote Sensing for Trasimeno lake Observatory (RESTO), positioned in a shallow and turbid lake in Central Italy, and the Acqua Alta Oceanographic Tower (AAOT), located 15 km offshore from the lagoon of Venice in the Adriatic Sea, which is characterised by clear to moderately turbid waters. 20 PRISMA images were available for the match-up analysis across both sites. Good performance of L2D was found for RESTO, with the lowest relative (Mean Absolute Percentage Difference, MAPD $< 25\%$) and absolute errors (Bias < 0.002) in the bands between 500 and 680 nm, with similar performance for ACOLITE. The lowest median and interquartile ranges of spectral angle (SA $< 8°$) denoted a more similar shape to the RESTO *in situ* data, indicating pigment absorption retrievals should be possible. ACOLITE showed better statistical performance at AAOT compared to L2D, providing $R^2 > 0.5$, Bias < 0.0015 and MAPD $< 35\%$, in the range between 470 and 580 nm, i.e. in the spectral range with highest reflectances. The addition of a SWIR based sun-glint correction to the default atmospheric correction implemented in ACOLITE further improved performance at AAOT, with lower uncertainties and closer spectral similarity to the *in situ* measurements, suggesting that ACOLITE with glint correction was able to best reproduce the spectral shape of *in situ* data at AAOT. We found good results for PRISMA Rrs retrieval in our study sites, and hence demonstrated the use of PRISMA for aquatic ecosystem mapping. Further studies are needed to analyse performance in other water bodies, over a wider range of optical properties.

1. Introduction

Hyperspectral remote sensing provides measurements across many narrow and spectrally contiguous bands, retrieving a continuous spectrum that can represent biogeophysical parameters and processes (Goetz et al., 1985). Earth observation by imaging spectroscopy has evolved in the last 30 years from a sparsely available research instrument into an operational technology accessible to a broad user community (Goetz, 2009; Schaepman et al., 2009). Inspired by the

* Corresponding author.
E-mail address: federica.braga@ismar.cnr.it (F. Braga).

https://doi.org/10.1016/j.isprsjprs.2022.08.009
Received 7 May 2022; Received in revised form 11 July 2022; Accepted 11 August 2022
Available online 19 August 2022

Nomenclature

Symbol	Description
AAOT	Acqua Alta Oceanographic Tower
AERONET	Aerosol Robotic Network
AERONET-OC	Aerosol Robotic Network - Ocean Colour
AHSI	Advanced Hyperspectral Imager
AOT	Aerosol Optical Thickness
ASI	Italian Space Agency
Cal/Val	Calibration and Validation activities
CHIME	Copernicus Hyperspectral Imaging Mission for the Environment
CHRIS	Compact High Resolution Imaging Spectrometer
d	sun-earth distance
DDV	Dense Dark Vegetation
DESIS	DLR Earth Sensing Imaging Spectrometer
DLR	Space Agency of the German Aerospace Center
DSF	Dark Spectrum Fitting
E_d	Downwelling irradiance
EnMAP	Environmental Mapping and Analysis Program
EO-1	Earth Observing-1
ESA	European Space Agency
F_0	mean extraterrestrial solar irradiance
FRM	Fiducial Reference Measurement
FWHM	Full Width at Half Maximum
GC	Glint Correction
GSD	Ground Sampling Distance
HDF-EOS5	Hierarchical Data Format - Earth Observing System
HICO	Hyperspectral Imager for the Coastal Ocean
HISUI	Japanese Hyperspectral Imager SUIte
ISS	International Space Station
L1	Level 1
L2	Level 2
L2-WFR	Level 2- Water Full Resolution
L_d	downwelling radiance
L_{TOA}	Top-Of-Atmosphere radiance
L_u	upwelling radiance
LUT	Look-Up Table
L_{wn}	normalised water-leaving radiances
MAD	Mean Absolute Difference
MAPD	Mean Absolute Percentage Difference
MERIS	Medium Resolution Imaging Spectrometer
MODIS	Moderate Resolution Imaging Spectroradiometer
NASA	National Aeronautics and Space Administration
$NE\Delta L_{TOA}$	Noise-Equivalent radiance difference
OLCI	Ocean and Land Colour Instrument
OSOAA	Ordres Successifs Océan Atmosphère
PACE	Plankton, Aerosol, Cloud, ocean Ecosystem
PAN	panchromatic
PANTHYR	Pan-And-Tilt HYperspectral Radiometer
PRISMA	PRecursore IperSpettrale della Missione Applicativa
RESTO	REmote Sensing for Trasimeno lake Observatory
RMSD	Root Mean Square Difference
Rrs	Remote sensing reflectance
S	Spherical albedo of the atmosphere
SA	Spectral Angle
SBG	Surface Biology and Geology
SHALOM	Spaceborne Hyperspectral Applicative Land and Ocean Mission
SNR	Signal-to-Noise Ratio
SWIR	Short-Wave Infrared
SZA	Solar Zenith Angle
t_d	total atmospheric transmittance in the sun-surface path
t_{gas}	gas transmittance
t_u	total atmospheric transmittance in the surface-sensor path
VIIRS	Visible Infrared Imaging Radiometer Suite
VNIR	Visible to Near InfRared
VZA	View Zenith Angle
WV	Water Vapor Columnar content
θ_s	per-pixel sun zenith angle
ρ_F	Fresnel reflectance factor
ρ_{path}	atmospheric path reflectance
ρ_s	surface level reflectance
ρ_{toa}	top-of-atmosphere reflectance
ρ_w	water-leaving reflectance

achievements of airborne hyperspectral imagery and a growing user demand, spaceborne hyperspectral sensors have taken a stride forward in advancing in payload technology, sensor performance and onboard calibration devices (Transon et al., 2018; Rast and Painter, 2019; Dierssen et al., 2021). The availability of the full spectrum from the visible through near-infrared (VNIR), and typically extending to the short-wave infrared (SWIR) wavelengths, has led to the definition of specific protocols for validation activities (e.g. Concha et al., 2021), to the implementation of robust atmospheric correction methodologies and new retrieval algorithms, as well as the derivation of innovative products and applications in terrestrial and aquatic ecosystems (Giardino et al., 2019; Rast and Painter, 2019; Lu et al., 2020).

In the first decade of the new millennium, spaceborne imaging spectrometers were launched as technology demonstration missions. In 2000, Hyperion, onboard NASA's Earth Observing-1 (EO-1) spacecraft, was the first imaging spectrometer to routinely acquire science-grade data from Earth orbit (Pearlman et al., 2003). Hyperion acquired hyperspectral images in the 400–2500 nm spectral range at 30 m spatial resolution and it was used in a variety of studies dealing with land and water applications (Brando and Dekker, 2003; Giardino et al., 2007; Pengra et al., 2007; Pignatti et al., 2009; George et al., 2014). In 2001, the Compact High-Resolution Imaging Spectrometer (CHRIS) was launched aboard ESA's PROBA-1 microsatellite (Barnsley et al., 2004). It acquires 13 square km scenes at 18–36 m spatial resolution in 18–62 user-selected VNIR spectral bands (400–1000 nm). Recently there was a renewed interest in CHRIS data for coastal water applications (Lavigne et al., 2021) as preparation for hyperspectral ocean colour missions. From 2009 to 2015, the Hyperspectral Imager for the Coastal Ocean (HICO), developed by NASA and the U.S. Office of Naval Research, operated onboard the International Space Station (Lucke et al., 2011). HICO provided imagery focused on aquatic targets with a 90 m spatial resolution in the VNIR spectral region and its data have been used in water quality studies (Braga et al., 2013; Moses et al., 2013; Keith et al., 2014; Dierssen et al., 2015; Ibrahim et al., 2018; Pahlevan et al., 2021a; Soppa et al., 2021). These hyperspectral missions were the main sources of hyperspectral satellite data for years, but the amount and the quality of data were quite insufficient for a wide range of potential applications (Guanter et al., 2015).

More recently, several hyperspectral missions have been launched, including the Space Agency of the German Aerospace Center (DLR) Earth Sensing Imaging Spectrometer (DESIS) onboard the International Space Station (ISS) (Krutz et al., 2019), China's Advanced Hyperspectral Imager (AHSI) aboard the GaoFen-5 satellite (Liu et al., 2019), and HyperScout-1, a smart hyperspectral imager for nanosatellites (Esposito and Marchi, 2019), all launched in 2018. The Japanese Hyperspectral Imager SUIte (HISUI) mission onboard the ISS (Matsunaga et al., 2019) and the PRecursore IperSpettrale della Missione Applicativa (PRISMA) sensor by the Italian Space Agency (ASI) (Loizzo et al., 2018), were

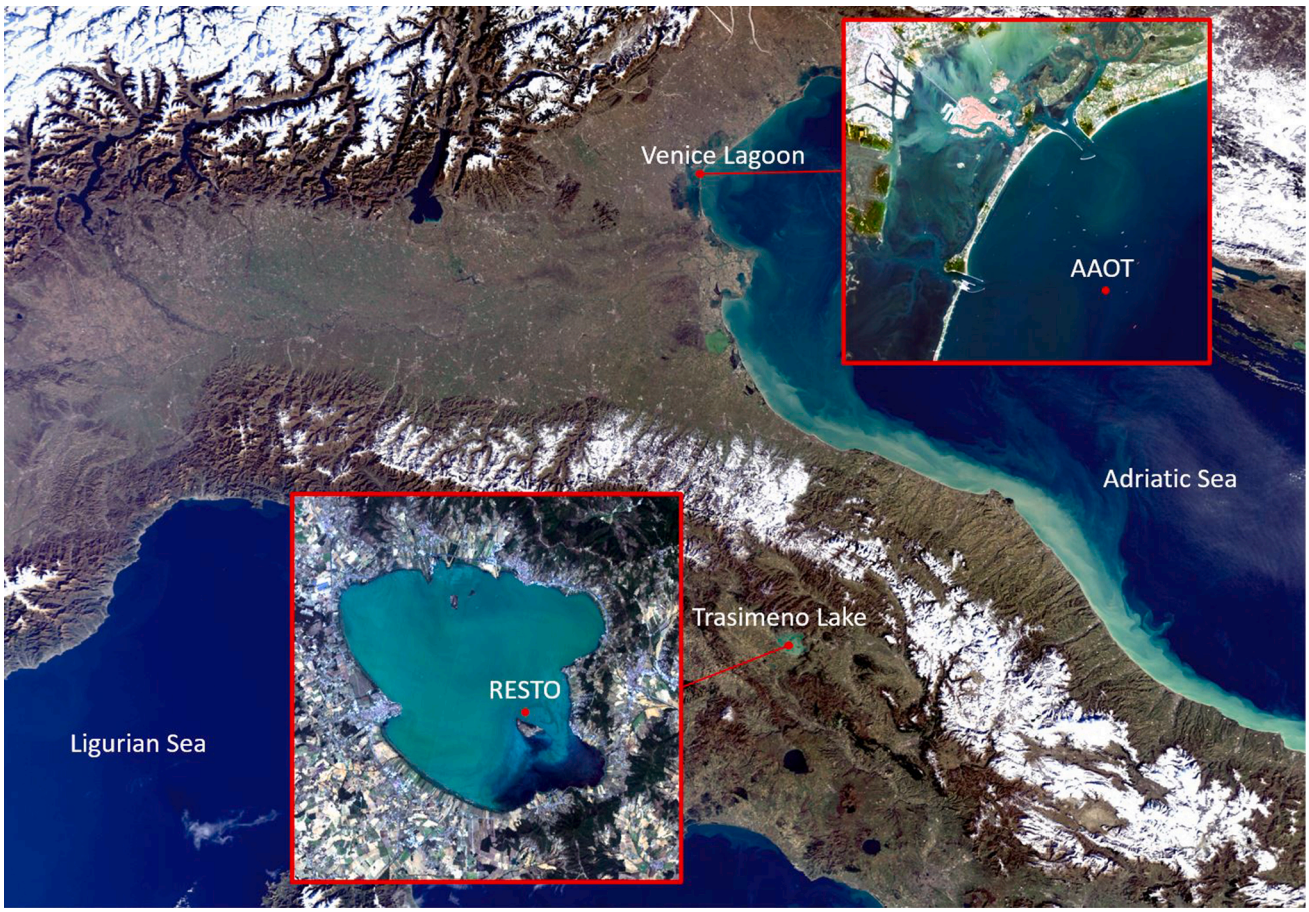

Fig. 1. S3/OLCI image of Northern and Central Italy. In the insets, two PRISMA images of the study area. Red dots show the position of Acqua Alta Oceanographic Tower (AAOT), located 15 km off the Venice lagoon in the northern Adriatic Sea, and the REmote Sensing for Trasimeno lake Observatory (RESTO) in Lake Trasimeno, where fixed autonomous instrumentations are mounted. (For interpretation of the references to color in this figure legend, the reader is referred to the web version of this article.)

launched in 2019 and the DLR Environmental Mapping and Analysis Program (EnMAP) (Guanter et al., 2015) launched in 2022. Moreover, the Israeli/Italian Spaceborne Hyperspectral Applicative Land and Ocean Mission (SHALOM) (Feingersh and Ben-Dor, 2015) and Italian PRISMA Second Generation (Formaro et al., 2021) are expected in 2025.

In support of the Calibration and Validation activities (Cal/Val) of the hyperspectral PRISMA mission, developed by ASI, Giardino et al. (2020) reported that PRISMA Top-Of-Atmosphere radiance (L_{TOA}) of Level 1 (L1) products is consistent with the expected values observable over water targets. In such a context, this work aims to provide a first assessment of PRISMA Level 2D Rrs products (as distributed by ASI) and ACOLITE derived Rrs over two optically diverse inland and coastal sites. ACOLITE was adapted for processing PRISMA L1 products as it has proven good performance for different multispectral sensors over various water types (Vanhellemont and Ruddick, 2018; Vanhellemont, 2019; Pahlevan et al., 2021b). PRISMA Rrs accuracy is assessed with a match-up analysis with above-water *in situ* reflectance measured by autonomous hyper- and multispectral radiometer systems mounted on fixed platforms. PRISMA data is also compared to operational satellite data using near-coincident S3/OLCI L2-Water Full Resolution (L2-WFR) products. Despite the spatial resolution of S3/OLCI being one order of magnitude lower than PRISMA, its high revisit time always ensured a match-up, while providing 15 spectral bands potentially matching those of PRISMA.

2. Challenges for spaceborne imaging spectrometry in aquatic environments

Although the capabilities of spaceborne imaging spectrometry in aquatic environments have been demonstrated in several case studies (Brando and Dekker, 2003; Giardino et al., 2007; Santini et al., 2010; Braga et al., 2013; Keith et al., 2014; Dierssen et al., 2015; Ibrahim et al., 2018; Niroumand-Jadidi et al., 2020; Pahlevan et al., 2021a; Soppa et al., 2021), there are crucial issues that remain unresolved in comparison to data from multispectral satellites, such as i) the availability of hyperspectral fiducial reference measurements (FRMs), ii) atmospheric correction, including the air–water interface effects; and iii) signal-to-noise ratio and the overall sensitivity of water reflectance.

Cal/Val activities with measurement networks and reference sites are fundamental to track sensor performance during its mission and to determine the quality and integrity of hyperspectral data products (Sterckx et al., 2020). The standardisation and quality control of reference datasets are necessary to support reliable activities on Cal/Val (Ruddick et al., 2019; Niro et al., 2021). In the context of FRMs of water reflectance for satellite validation, autonomous *in situ* radiometer systems can provide improved representative data for match-up analysis (Zibordi et al., 2012; Donlon and Zibordi, 2014; Ruddick et al., 2019). A prime example is the Aerosol Robotic Network - Ocean Colour (AERONET-OC) (Zibordi et al., 2009a; Zibordi et al., 2020): by collecting consistent and accurate multispectral measurements of normalised water-leaving radiance, it represents the main source of validation data for past and current spaceborne optical missions, such as the Medium

Resolution Imaging Spectrometer (MERIS), the Moderate Resolution Imaging Spectroradiometer (MODIS), the Visible Infrared Imaging Radiometer Suite (VIIRS), and the Sentinel-3 Ocean and Land Colour Instrument (S3/OLCI) (e.g. Valente et al., 2019; Concha et al., 2021; Cazzaniga et al., 2022; Zibordi et al., 2022). Autonomous hyperspectral radiometer systems have recently been developed and deployed on fixed platforms (e.g. Peters et al., 2018; Vansteenwegen et al., 2019) or ships (e.g. Simis and Olsson, 2013; Brando et al., 2016; Giannini et al., 2021; Tilstone et al., 2021) and can cover the validation of VNIR bands of present and future satellite hyperspectral missions. The significant advantage of autonomous hyperspectral radiometers in providing validation data was demonstrated for S3/OLCI (Vanhellemont and Ruddick, 2021), PRISMA (Giardino et al., 2020; Bresciani et al., 2022), DESIS (Bresciani et al., 2022) and CHRIS-PROBA (Lavigne et al., 2021).

The quality of surface parameter retrievals strongly depends on successful removal of the atmospheric contributions to the signal measured by satellite sensors, including the air–water interface effects for water targets. Atmospheric radiative transfer modelling and inversion techniques are challenging when measurements include absorbing bands, as in the case of hyperspectral sensors observing in the entire visible spectrum (Gao et al., 2000; Guanter et al., 2007; Bassani et al., 2015; Giardino et al., 2019; Thompson et al., 2019). For satellite observations of open ocean waters, the contribution of atmospheric path radiance in the VNIR spectrum represents up to 90% of at-sensor radiance (Gordon, 1978; Antoine and Morel, 1999) caused predominantly by scattering in the atmosphere, with significant variability due to aerosol concentration and type. Other issues affecting the retrieval of surface reflectance over inland and coastal water may also be taken into account, such as sun-glint reflectance, high turbidity or bottom visibility with non-zero water reflectance in the near infrared, and the proximity of land (adjacency effects) (Frouin et al., 2019).

Another technical constraint is represented by the Signal-to-Noise Ratio (SNR), which is lower for hyperspectral sensors than for multispectral sensors, as a result of the trade-off between the narrow bandwidth of the spectral channels and the required energy to illuminate detector elements (Moses et al., 2012; Transon et al., 2018). The SNR has a significant impact on at-sensor radiance, atmospherically corrected surface-level reflectance, and therefore, on the derived biogeophysical parameters, affecting the overall sensitivity for detecting changes in radiance or reflectance and the accuracy for retrieving environmental variables (Brando and Dekker, 2003). This is specifically critical in imaging spectrometry of aquatic environments, which are highly absorptive and whose radiometric contribution to the at-sensor radiance is small compared to the total radiance measured by the sensor, in particular for the blue bands which have a large contribution from atmospheric path radiance (IOCCG, 2000; Brando and Dekker, 2003; Wettle et al., 2004; Moses et al., 2012).

Addressing these challenges will prepare for the forthcoming operational spaceborne hyperspectral missions. ESA and NASA have identified hyperspectral missions as key to addressing important scientific and environmental management objectives: for instance, the NASA's Plankton, Aerosol, Cloud, ocean Ecosystem (PACE) (Werdell et al., 2019) and Surface Biology and Geology (SBG) (Cawse-Nicholson et al., 2021) missions, or the Copernicus Hyperspectral Imaging Mission for the Environment (CHIME) under development by the European Commission and ESA. The common aim of the PACE, SBG and CHIME missions is to provide imaging spectroscopy data at global coverage and regular frequency with high spatial resolution in the mid-to-late 2020s.

3. Data and methods

3.1. Study area and in situ radiometric data

The FRMs of water reflectance used in this study and acquired in coincidence to PRISMA images were gathered from fixed autonomous instruments, respectively placed in a coastal and in a lacustrine site in Italy (Fig. 1). The coastal site corresponds to the Acqua Alta Oceanographic Tower (AAOT), located 15 km off the Venice lagoon in the northern Adriatic Sea (12.51° E, 45.31° N), representing a historic AERONET-OC site and, recently, a WATERHYPERNET network site. AAOT is an offshore laboratory purpose-built in 1975 to support coastal research (Cavaleri, 2000) and has been used to support ocean colour validation activities through a comprehensive collection of bio-optical and radiometric data since 1995 (Berthon and Zibordi, 2004; Zibordi et al., 2004a; Zibordi et al., 2004b; Mélin et al., 2007). The site is in a transitional region between open sea and coastal waters and it is characterised by both Case-1 and Case-2 waters, with an occurrence of roughly 35% Case-2 waters moderately dominated by sediments (Berthon and Zibordi, 2004; Zibordi et al., 2009b). The aerosol type, occasionally maritime, is mostly continental due to atmospheric inputs from the close Padana Plain (Zibordi et al., 2004a; Zibordi et al., 2006).

The lacustrine site corresponds to Lake Trasimeno (12.10° E, 43.13° N), a shallow turbid lake of Central Italy, where the REmote Sensing for Trasimeno lake Observatory (RESTO) is equipped with a WISPStation (Peters et al., 2018), operating since 2018 and supporting a variety of applications (Bresciani et al., 2020; Free et al., 2021; Free et al., 2022). The RESTO station is representative of Case-2 waters that, in spite of the shallow bathymetry, are always optically deep. Wind-induced sediment resuspension frequently occurs and the high nutrient availability facilitates the occurrence of phytoplankton blooms, including cyanobacteria species typically appearing from late summer to early autumn (Bresciani et al., 2020; Free et al., 2021).

3.1.1. Acqua Alta Oceanographic Tower

At the AAOT, *in situ* radiometry was collected with two systems: the Pan-And-Tilt HYperspectral Radiometer (PANTHYR) (Vansteenwegen et al., 2019), and the multispectral AERONET-OC. PANTHYR, which is operating since September 2019, is part of the WATERHYPERNET network (https://waterhypernet.org/) and consists of two TriOS-RAMSES hyperspectral radiometers, mounted on a pan-and-tilt pointing system, controlled by a single-board-computer and custom-designed electronics which provide power, pointing instructions, and data archiving and transmission. It autonomously acquires hyperspectral Rrs every 20 min during daytime at programmed relative azimuth angles to the Sun.

PANTHYR sequentially measures the hyperspectral irradiance (E_d, 3 replicates), downwelling radiance (L_d, 3 replicates), upwelling radiance (L_u, 11 replicates), L_d (3 replicates), and E_d (3 replicates). Measurements were calibrated, dark current corrected, and resampled to a common wavelength grid, from 350 to 900 nm at 2.5 nm steps. Individual scans were subjected to a quality control as in Ruddick et al. (2006) and then averaged to provide a single equivalent measurement if sufficient replicates pass quality control (5/6 for E_d and L_d, 9/11 for L_u). Rrs were computed from the averaged L_u, E_d, and L_d using the Mobley (1999) modelled effective Fresnel reflectance factor (ρ_F) for a fixed 2 m s^{-1} wind speed. Final measurement quality checks for sky and water variability are also performed as in Ruddick et al. (2006), i.e. excluding data with the coefficient of variation of $\rho_w(780\text{ nm}) > 10\%$ and $L_d/E_d(750\text{ nm}) > 5\%$. In the present study, data acquired at 270° relative azimuth angle were used (Vanhellemont, 2020).

The multispectral radiometric measurements were obtained from the AERONET-OC (https://aeronet.gsfc.nasa.gov/new_web/ocean_color.html), an autonomous system for satellite ocean color validation activities, based on the SeaPRISM version of the CE-318 sun-photometer (Zibordi et al., 2004b; Zibordi et al., 2009a; Zibordi et al., 2020). Quality-assured (Level 2.0) and cloud cleared and quality controlled (Level 1.5) normalised water-leaving radiances (L_{wn}), corrected for bidirectional effects with f/Q approach (Morel et al., 2002), were selected for the 2019–2020 and 2021, respectively. Level 2.0 data ensure the highest quality for validation analysis, but Level 1.5 data may also be used for Near Real Time evaluations of satellite missions (Bracaglia et al., 2019; Vanhellemont, 2019; Bracaglia et al., 2020; Concha

Table 1
Data overview for AAOT match-up analysis of PRISMA, S3-A and S3-B/OLCI, and *in situ* measurements. VZA indicates the View Zenith Angle of PRISMA. Wind speed recorded at AAOT, Solar Zenith Angle (SZA) and Aerosol Optical Thickness (AOT) at 550 nm from AERONET network, at the time of PRISMA overpasses are also reported in the table. *Collection 002, processing v.6.13. (Blank cells mean no data available).

Date (dd/mm/yyyy)	AOT 550 AERONET (-)	Wind speed ($m\ s^{-1}$)	SZA (Deg)	VZA (Deg)	Acquisition UTC Time (hh:mm)				
					PRISMA	AERONET-OC	PANTHYR	S3-A/OLCI	S3-B/OLCI
14/07/2019	0.0997	1.3	27.56	14.59	10:06	10:21		09:02*	
08/02/2020	0.2618	2.1	62.79	10.38	10:10	10:37	10:00		09:44
02/07/2020	0.1984	1.5	25.87	9.26	10:10		10:00	09:24	
25/07/2020	0.0786	5.0	29.61	15.61	10:06		10:00	09:28	
29/08/2020	0.2067	8.0	38.53	9.36	10:10		10:00	09:20	
09/03/2021	0.1719	10.8	51.61	9.96	10:17	11:55		09:43	09:03
09/06/2021	0.1993	3.2	26.15	16.07	10:03	10:16	10:00		09:18
06/08/2021	0.1208	4.6	32.43	15.16	10:04		10:00	09:54	09:15
12/08/2021	0.1688	3.2	33.75	9.97	10:07		10:00	08:58	10:00
10/09/2021	0.1513	3.9	42.57	8.34	10:07	08:42	10:00	09:46	09:07
15/10/2021	0.0735	4.3	54.93	2.02	10:11	12:30	10:00	09:39	09:00
06/12/2021	0.0313	5.6	68.87	8.71	10:08	11:15	10:00		09:52

et al., 2021). L_{wn} were converted to Rrs by dividing by F_0, the mean extraterrestrial solar irradiance (Thuillier et al., 2003). The AERONET-OC dataset was available in 6 spectral bands (central wavelengths: 412, 443, 490, 532, 551 and 667 nm) with a 10 nm bandwidth. Aerosol optical thickness (AOT) was gathered from the AERONET AAOT site (https://aeronet.gsfc.nasa.gov) (Holben et al., 1998; Holben et al., 2001). The AERONET AAOT site does not have a 550 nm channel and AOT at 550 nm was calculated by linear interpolation in log scale from two measurements at adjacent wavelengths.

3.1.2. *Remote sensing for Trasimeno lake Observatory*

At the RESTO, *in situ* radiometry was obtained every 15 min from a WISPStation, placed on a platform at 400 m from one of the main islands of Lake Trasimeno.

The WISPStation is an autonomous radiometer system that contains two sets of sensors looking at north-northwest and north-northeast, providing viewing geometries consistent with recommendations in Mobley (1999) to avoid sun-glint. It measures both the radiances (L_u and L_d angles are around 42° from the nadir and from the zenith, respectively) and irradiance near instantaneous at high frequency in the spectral range of 350–900 nm with a spectral resolution of 4.6 nm (Full Width at Half Maximum - FWHM). Rrs was calculated as described for the PANTHYR. The backend WISPcloud automatically selects one of the pair of observations best oriented with respect to the Sun azimuth at any time of the day, eliminating the need for moving parts. Recorded data are transmitted to the database ("WISPcloud") autonomously through a 3G connection. More details can be found in Peters et al. (2018) and Bresciani et al. (2020).

3.2. *Satellite data*

PRISMA is a scientific and demonstrative mission, operated by ASI. It was launched on 22 March 2019 and placed in a low Earth Sun-synchronous orbit, approximately at an altitude of 614.8 km, with a repeat cycle of 29 days. Thanks to the off-nadir pointing capability, the revisit time for a specific area can be reduced to less than one week. The PRISMA payload includes a hyperspectral sensor with VNIR and SWIR detectors with a Ground Sampling Distance (GSD) of 30-m and a co-registered 5-m panchromatic (PAN) camera. The imaging spectrometer acquires a hyperdata cube in a continuum of 238 spectral bands ranging from 400 to 2500 nm, with about 12-nm spectral resolution (Cogliati et al., 2021). A comprehensive description of the PRISMA optical design, technical specifications and pre-launch/in-flight spectral and radiometric calibration is available on Coppo et al. (2020). Access to mission capabilities is available through the ASI portal (https://prisma.asi.it/) and four different products are systematically produced by the ground processor: PRISMA L1 Top-Of-Atmosphere radiance (L_{TOA}) radiometrically corrected and calibrated; Level 2B/C/D geolocated and geocoded atmospherically corrected images. The L1 processor converts Level 0 raw imagery to L_{TOA} using a look-up table (LUT) transfer function from digital numbers to physical radiance units ($mW\ m^{-2}\ sr^{-1}\ nm^{-1}$). The L1 products' consistency with respect to FRMs for both water and terrestrial targets was resulting in-line with mission requirements and indicate that acquired images are suitable for further scientific applications (Giardino et al., 2020; Cogliati et al., 2021; Pignatti et al., 2022; Tagliabue et al., 2022). Level 2 processor converts L1 L_{TOA} to Bottom-of-Atmosphere Radiance or Reflectance. Details can be found in the PRISMA Algorithm Theoretical Basis Document (ASI, 2021).

For this study, which aims to report on the quality of the L2D processing, 20 cloud-free PRISMA images, acquired over AAOT (12 images) and RESTO (8 images) from July 2019 to December 2021, were selected (Table 1 and Table 2). L1 and L2C/D products, of which L2C merely needed as providing the viewing geometry needed to run ACOLITE, were downloaded from the mission website and converted from original HDF-EOS5 (Hierarchical Data Format - Earth Observing System) file to

Table 2
Data overview for RESTO match-up analysis of PRISMA, S3-A and S3-B/OLCI, and *in situ* measurements. Wind speed was obtained from local meteorological stations. VZA indicates the View Zenith Angle of PRISMA. Solar Zenith Angle (SZA), at the time of PRISMA overpass, is also reported in the table. *Collection 002, processing v.6.13. (Blank cells mean no data available).

Date (dd/mm/yyyy)	Wind speed ($m\ s^{-1}$)	SZA (Deg)	VZA (Deg)	Acquisition UTC Time (hh:mm)			
				PRISMA	WISPStation	S3-A/OLCI	S3-B/OLCI
08/07/2019	1.6	25.8	18.6	10:03	10:00	09:58*	
26/07/2019	1.8	27.3	0.9	10:13	10:15		09:17*
23/04/2020	3.4	33.5	19.3	10:04	10:00	09:39	
03/06/2020	3.4	24.0	6.2	10:11	10:15		09:37
25/07/2020	2.1	27.9	12.9	10:07	10:00	09:28	
30/11/2020	2.3	65.7	0.7	10:13	10:15	09:09	
09/06/2021	2.5	24.4	13.2	10:04	10:00		09:18
06/12/2021	4.4	66.8	6.4	10:08	10:00		09:52

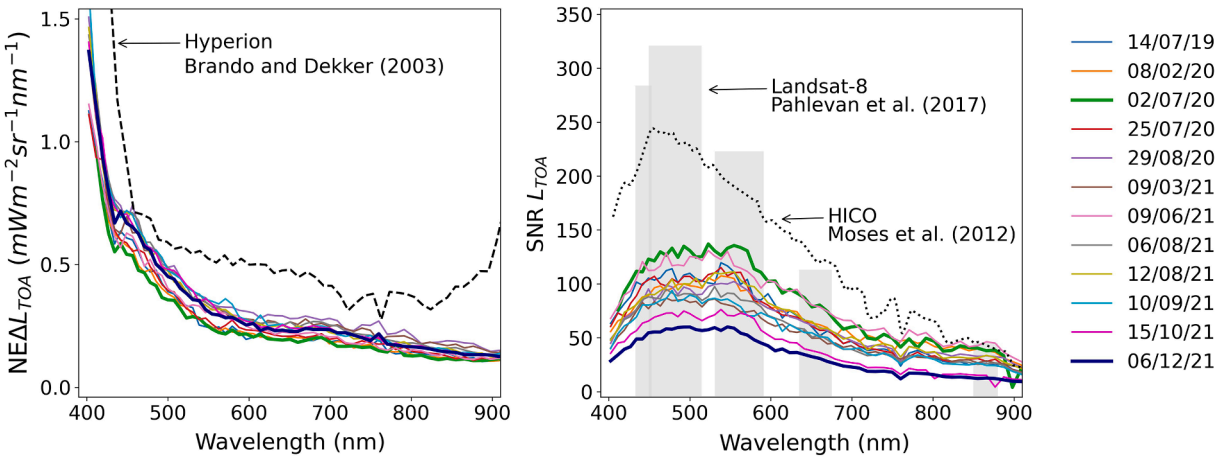

Fig. 2. Noise-equivalent radiance difference (on the left) and signal-to-noise ratio (on the right) derived from PRISMA L_{TOA} calculated over AAOT, according to Brando and Dekker (2003) and Wettle et al. (2004). Thicker lines indicate the scenes with maximum (blue line, 68.87° - December 6, 2021) and minimum SZA (green line, 25.87° - July 2, 2020). Dashed black line is the $NE\Delta L_{TOA}$ calculated for Hyperion in Brando and Dekker (2003). Dotted black line is the SNR estimated for HICO by Moses et al. (2012). Grey bars are SNR values for Landsat-8 derived from Pahlevan et al. (2017). (For interpretation of the references to color in this figure legend, the reader is referred to the web version of this article.)

band sequential file format using ENVI 5.6 (L3Harris Technologies, USA). Since strong improvements of the mission ground processor and the data product quality were achieved from the launch, we used L1 and L2C/D data processed by the last standard PRISMA mission ground processor version 3.9–2 and atmospheric correction processor version 2.05, respectively (ASI, 2021).

Sentinel-3 OLCI images corresponding to PRISMA overpasses were downloaded for a direct comparison with PRISMA data. S3/OLCI imagery for the North Adriatic Sea and for Lake Trasimeno were retrieved as baseline water products (L2-WFR), version 7.00 and downloaded from the Copernicus Online Data Access hosted by EUMETSAT (coda.eumetsat.int). Standard masking was used, i.e. excluding INVALID, LAND, CLOUD and CLOUD_AMBIGUOUS pixels.

3.3. Radiometric analysis

To assess on-orbit radiometric performance of PRISMA over water targets, the overall sensitivity of the entire sensor–atmosphere–water surface system for detecting changes in radiance was estimated. Two image-based parameters were considered in the analysis: the environmental noise-equivalent radiance difference ($NE\Delta L_{TOA}$) and the radiance signal-to-noise ratio (SNR L_{TOA}). These parameters were dependent on the nominal instrument SNR with added influences of noise in the image data due to observation geometry, atmospheric variability and thin clouds, water surface (with swell-, wave-, and wavelet-induced reflections) and refraction of diffuse and direct sky and sunlight (Brando and Dekker, 2003; Moses et al. 2012; Pahlevan et al., 2017).

The procedure described in Brando and Dekker (2003) and Wettle et al. (2004) was applied to imagery acquired by PRISMA over AAOT only, as PRISMA data over RESTO were not offering large homogenous areas of optically deep water as required for the analysis.

The $NE\Delta L_{TOA}$ was calculated from the PRISMA L1 L_{TOA}, according to Brando and Dekker (2003) and Wettle et al. (2004):

$$NE\Delta L_{TOA} = \sigma(L_{TOA}) \quad (1)$$

where $\sigma(L_{TOA})$ is the standard deviation in each band over a homogenous area of optically deep water within the image. The SNR L_{TOA} was calculated from the L_{TOA}, in the same area used for $NE\Delta L_{TOA}$, according to Moses et al. (2012):

$$SNR\ L_{TOA} = \frac{L_{TOA}}{NE\Delta L_{TOA}} \quad (2)$$

$NE\Delta L_{TOA}$ and SNR L_{TOA} were retrieved for a 21 × 21 pixels area over AAOT in different seasons and with SZA ranging within the 25°–69° range. As can be seen in Fig. 2, the spectra of $NE\Delta L_{TOA}$ and SNR L_{TOA} had similar shape and different magnitude. SNR L_{TOA} values are higher in the range between 440 and 640 nm and their variability lies between the curves associated with the lowest and the highest SZA (25.87° - July 2, 2020, 68.87° - December 6, 2021, respectively). SNR L_{TOA} varies with the SZA and increases at low SZA according to Moses et al. (2012). $NE\Delta L_{TOA}$ values are almost spectrally flat between 554 and 900 nm (average value of 0.25) and gradually increase to the Blue. Bands centred at 402, 411 and 419 nm are very noisy and this should be taken in account when assessing L2 data, because the environmental noise-equivalent affects the uncertainty of the retrieved products. $NE\Delta L_{TOA}$ associated with the lowest SZA is slightly lower across nearly all bands, while $NE\Delta L_{TOA}$ for the two scenes acquired with wind speed above 8 m s^{-1} is a bit higher in the Red and NIR region.

$NE\Delta L_{TOA}$ curves calculated for PRISMA are lower than that reported for Hyperion in Brando and Dekker (2003): this suggests that PRISMA has improved radiometric sensitivity, given that PRISMA and Hyperion have very similar sensor design with the same spatial (GSD = 30 m) and spectral resolution (about 10 nm). The PRISMA SNR L_{TOA} ranged 100–120 in the 450–600 nm spectral range (Fig. 2), half of SNR L_{TOA} values of HICO (Moses et al., 2012) and Landsat-8 (Pahlevan et al., 2017). However, Landsat-8 consists of 5 wider spectral bands in the VNIR, while PRISMA has 66 narrow contiguous spectral bands within the VNIR region, containing more environmentally meaningful information for the characterization of optically complex coastal/inland waters (Dierssen et al., 2021). Compared to the hyperspectral sensor HICO, PRISMA offers a finer GSD (HICO's GSD is about 90 m at nadir), enabling the mapping of smaller inland aquatic areas and nearshore waters. Furthermore, the requirements for ocean colour missions are SNR > 600 for the NIR bands and > 1000 for the UV–VIS bands (Hu et al., 2012; Mouw et al., 2015) while future imaging spectrometers will have SNR > 400 in the VNIR (NASEM, 2018). This seems to suggest that techniques to improve the SNR L_{TOA} might be required for specific applications which need higher values of SNR. Recognizing that the SNR L_{TOA} is proportional to the square root of the area of a pixel (Brando and Dekker, 2003; Schott, 2007), spatially aggregated 60 or 90 m PRISMA imagery should offer adequate radiometric quality.

3.4. Atmospheric correction processors

3.4.1. Standard L2D processor

The Level 2 standard atmospheric correction processor is based on MODTRAN v6.0, using a multi-dimensional LUT approach. A comprehensive description of the algorithms used for the generation of the PRISMA products L1 and L2B/C/D is available in ASI (2021). The atmospherically corrected dataset is generated starting from the L1 product, with related metadata, and auxiliary data, including the LUTs. The LUT entails simulated L_{TOA}, obtained through a radiative transfer model. L_{TOA} is pre-computed, stored and indexed as a function of geometric condition (sun zenith angle, relative azimuth angle and view zenith angle) and different atmospheric scenario based on atmospheric model (mid-latitude winter and summer), ground altitude, water vapour, and aerosol optical thickness. Results from simulations are stored in LUTs and the atmospheric correction processor reads the LUTs pertaining to each parameter space and interpolates if required. The aerosol model used to build LUTs is limited to the rural model provided by MODTRAN6 library.

The Level 2 processor estimates the amount of Water Vapor Columnar content (WV) and Aerosol Optical Thickness (AOT). The WV retrieval over land is performed with the atmospheric precorrected differential absorption algorithm (Kaufman et al., 1997), which compares the reflected solar radiation in the absorption channel (e.g. 940 nm) with the reflected solar radiation in nearby non-absorption channels. The retrieval of AOT is based on the Dense Dark Vegetation (DDV) algorithm approach, exploiting the correlation between reflectances in the SWIR region and the blue and red bands. If the scene contains no dark pixels suitable for the retrieval of AOT, the atmospheric correction processor uses a default constant value. Finally, the atmospheric inversion procedure is performed to derive the at-surface atmospherically corrected spectral reflectance.

Surface reflectance Level 2C product also contains auxiliary maps related to: concentration of the columnar atmospheric water vapour and, where possible, the maps related to AOT and Angstrom exponent. Surface reflectance Level 2D products are directly used for application purposes since they already contain geophysical and geo-coded information. PRISMA surface reflectance Level 2D products were converted to remote sensing reflectance by dividing by π and were used for comparison (ASI, 2021); for sake of clarity, we will refer to these products still as L2D, despite the use of π.

3.4.2. ACOLITE processor

ACOLITE was primarily designed for processing multispectral images for aquatic remote sensing applications and it was now adapted to support processing of PRISMA L1 data. ACOLITE uses the dark spectrum fitting (DSF) algorithm (Vanhellemont and Ruddick, 2018) to estimate the aerosol optical thickness (AOT) and hence atmospheric path reflectance (ρ_{path}), transmittances and spherical albedo. The ACOLITE/DSF processing of PRISMA data is included in the publicly available GitHub code and in binary releases since 20210802.0 (both distributed through https://github.com/acolite/acolite).

For ACOLITE/DSF processing the PRISMA L1 and matching L2C data are required as inputs. At runtime, band specific Gaussian relative spectral response functions are generated for both VNIR and SWIR detectors, using the central wavelength and FWHM information provided in the HDF5 metadata. Geometry information is currently not included in the L1 data, and hence the per-pixel sun and view geometry (i.e. sun and view zenith and relative azimuth angles) is extracted from the matching L2C file.

L_{TOA} are computed from the 16 bit unsigned integer data using the offset and scale factors in the HDF5 metadata:

$$L_{TOA} = offset + DN/scale \quad (3)$$

L_{TOA} is converted to top-of-atmosphere reflectance (ρ_{TOA}) by:

$$\rho_{TOA} = (L_{TOA} * \pi * d^2)/(F_0 * cos\theta_s) \quad (4)$$

where F_0 is the band averaged extraterrestrial solar irradiance (Thuillier et al., 2003), d the sun-earth distance in astronomical units, and θ_s the scene averaged or per-pixel sun zenith angle. Ancillary or user set values for atmospheric ozone and water vapour content are used to perform a gas transmittance (t_{gas}) correction to the PRISMA ρ_{TOA}:

$$\rho'_{TOA} = \frac{\rho_{TOA}}{t_{gas}} \quad (5)$$

Next to variable ozone and water vapour concentrations, the t_{gas} correction includes constant concentrations of oxygen, carbon dioxide, nitrous oxide, and methane. Bands with low t_{gas} are excluded from further processing, i.e. bands with $t_{gas} < 0.85$ are excluded from AOT estimation, and bands with $t_{gas} < 0.75$ are excluded from surface level reflectance (ρ_s) calculation. ρ'_{TOA} is then modelled according to Vermote et al. (1997):

$$\rho'_{TOA} = \rho_{path} + (\rho_s * t_u * t_d)/(1 - \rho_s * S) \quad (6)$$

where ρ_{path} is the atmospheric path reflectance (combining Rayleigh and aerosols), t_d and t_u are the total atmospheric transmittances in the sun-surface and surface-sensor paths, and S the spherical albedo of the atmosphere. The atmospheric correction is performed using the LUTs of Vanhellemont (2020), with 82 wavelength steps, i.e. of 10 nm from 380 to 900 nm, 100 nm from 900 to 1500 nm, and 50 nm for 1500–2400 nm. These LUTs require inputs of aerosol model, AOT, atmospheric pressure, and the sun and view geometry, of which the first two need to be estimated.

The AOT and aerosol type are considered to be fixed over the 30 × 30 km PRISMA acquisition, and are estimated from the image itself. For two aerosol models, the continental and maritime model from 6SV (Vermote et al., 1997), the AOT is estimated from the 1st percentile of the ρ'_{TOA} observations in every band between 500 and 970 nm. The 1st percentile of ρ'_{TOA} is assumed to be equal to ρ_{path}, i.e. $\rho_s = 0$, giving an estimate of AOT in each band. Per aerosol model, the lowest AOT estimate is selected, and finally the aerosol model giving the best fit between the two bands giving the lowest AOT estimates is retained for further processing. For this aerosol model and AOT, the LUT is interpolated to the per-pixel sun and view geometry. The LUT outputs are resampled to the spectral response function of each PRISMA spectral band, and then ρ_s can be computed. Remote sensing reflectance is output by dividing the corrected ρ_s by π. Hereafter we will refer to Rrs obtained from the ACOLITE atmospheric correction of PRISMA L1 as ACOLITE/DSF.

In the present study, an optional residual air–water interface reflectance correction is performed on the ρs retrieval. This correction is performed by estimating the interface reflectance signal in the SWIR from the average ρs between 1500 and 2400 nm - i.e. assuming zero water leaving radiance in this spectral range. To extend this average SWIR observation towards the VNIR, the interface reflectance is modelled with OSOAA (Chami et al., 2015) for the current scene average sun-sensor geometry, the estimated aerosol model and AOT for a high (20 m s^{-1}) wind speed (Vanhellemont, 2020; Vanhellemont and Ruddick, 2021). A scaling factor is computed from the ratio of the average modelled interface reflectance between 1500 and 2400 nm and the observed SWIR reflectance. The full interface reflectance spectrum is then scaled with this factor and subtracted from the ρ_s. Remote sensing reflectance is output by dividing the air–water interface reflectance corrected ρ_s by π and hereafter we will refer to it as ACOLITE/DSF + GC.

3.5. Match-up analysis

The extraction of PRISMA spectra from L2D and ACOLITE products was based on the characteristics of the platform providing hyperspectral FRMs. For AAOT, where the radiometric impact of the platform and its

Table 3
Statistical metrics used to assess the agreement of Rrs among the datasets; n is the number of concurrent observations of the match-up, and x_i and y_i are the *in situ* and PRISMA-estimated Rrs data, respectively.

Coefficient of determination R^2	$R^2 = \left[\frac{\sum_{i=1}^{n}(x_i-\bar{x})(y_i-\bar{y})}{\sqrt{\sum_{i=1}^{n}(x_i-\bar{x})^2}\sqrt{\sum_{i=1}^{n}(y_i-\bar{y})^2}}\right]^2$
Root Mean Square Difference (RMSD)	$RMSD = \sqrt{\frac{\sum_{i=1}^{n}(y_i-x_i)^2}{n}}$
Bias	$Bias = \frac{\sum_{i=1}^{n}(y_i-x_i)}{n}$
Mean Absolute Difference (MAD)	$MAD = \frac{\sum_{i=1}^{n}\lvert y_i-x_i\rvert}{n}$
Mean Absolute Percentage Difference (MAPD)	$MAPD = \frac{100}{n}\sum_{i=1}^{n}\left\lvert\frac{y_i-x_i}{x_i}\right\rvert$
Spectral Angle (SA)	$SA = \cos^{-1}\frac{\sum_{i=1}^{n}y_i x_i}{\sqrt{\sum_{i=1}^{n}y_i^2}\sqrt{\sum_{i=1}^{n}x_i^2}}$

shadows as well as the white caps caused by the structure-induced turbulence can disturb the validation window, a 10 × 10 pixels frame excluding the centre portion of the extract was used to avoid platform-induced contamination, similar to Ilori et al. (2019). For RESTO, a 3 × 3 pixels window centred on the location of the station was used in continuity with previous studies (Giardino et al., 2020; Bresciani et al., 2020; Giardino et al., 2021), assuming that platform size does not impact on the remotely sensed radiometry. A spatial homogeneity check over the pixel values in the satellite extract was performed to exclude measurements of insufficient quality, similarly to Bailey and Werdell (2006). The filtered mean value of the extract was used for the match-ups, i.e. considering only the pixel values that fell between the median ± 1.5* standard deviation, evaluated on the pixels box. Due to the coarser spatial resolution of S3/OLCI (300 m) with respect to PRISMA (30 m), a single pixel containing the station coordinates was extracted from the S3/OLCI satellite data.

Although a time window between ± 1 and ± 3 h between FRMs and satellite data has been considered usually adequate for match-up analysis in inland and coastal waters (Bailey and Werdell, 2006; Zibordi et al., 2009b; Guanter et al., 2010), the availability of high-frequency measurements for AAOT and RESTO allowed a time window of ± 15 mins to further reduce uncertainties related to time differences between the two observations (Vanhellemont and Ruddick, 2021).

At first, a qualitative comparison of reflectance of PRISMA Rrs as derived from L2D and ACOLITE, *in situ* data and S3-A and S3-B/OLCI, at their original spectral resolutions, was performed in the range of 400–800 nm. A second comparison of resampled *in situ* hyperspectral data and PRISMA spectra was performed for each site. To this aim, PANTHYR and WISPStation measurements were spectrally resampled to the FWHM of PRISMA bands covered by the *in situ* instruments.

A set of descriptive statistics to assess the consistency between Rrs of PRISMA (L2D and ACOLITE) and the reference dataset was calculated: the square of the Pearson correlation (R^2, the coefficient of determination), the Root Mean Square Difference (RMSD), the Bias, the Mean Absolute Difference (MAD), the Mean Absolute Percentage Difference (MAPD), the Spectral Angle (SA) (Table 3). The SA was used to determine how similar the shape of PRISMA spectra is to *in situ* FRM. SA (0-180°) is calculated in the spectral range for 410 to 770 nm and a lower SA indicates higher similarity.

4. Results and discussion

In the period from July 2019 to December 2021, 20 PRISMA images with synchronous FRMs were available for the match-up analysis. Spectral match-ups were distributed as follows: 7 from AERONET-OC and 10 from PANTHYR for AAOT, and 8 from WISPStation for RESTO. The sensing time of FRMs from the different sources and PRISMA data is provided in Table 1 and Table 2 for AAOT and RESTO, respectively. S3/OLCI images acquired on the same day of PRISMA are also listed.

As expected, the reflectance spectra of FRM between the sites differed greatly in magnitude and shape, due to very different characteristics of the sites and large optical diversity of the two water bodies (Fig. 3). Overall, AAOT exhibited a local maximum around 500 nm and non-negligible values in the 650–700 nm range, typical of clear oligotrophic water, slightly influenced by suspended particles. RESTO showed the local maxima at 563 nm, with the distinct Chlorophyll-a (Chl-a) feature around 675–690 nm, typical of meso- and eu-trophic conditions; the influence of phycocyanin near 620–630 nm can also be recognised in the Rrs spectra (Fig. 3). A significant variability in magnitude and spectral shape was also visible in both sites, caused by the wide range of bio-optical properties influenced by seasonal conditions and meteorological forcing. Overall, the Rrs spectra are representative of the variability observed at AAOT in Zibordi et al. (2020) and at Lake Trasimeno in Bresciani et al. (2020). Compared to AERONET-OC, both PANTHYR and RESTO provided continuous spectra with many narrow and spectrally contiguous bands, enabling the validation of all 66 PRISMA bands in the VNIR range.

The qualitative comparison of the FRMs and Rrs spectra of L2D and ACOLITE derived from PRISMA and from S3/OLCI at their original spectral resolutions is shown in Fig. 4 and Fig. 5 for AAOT and RESTO

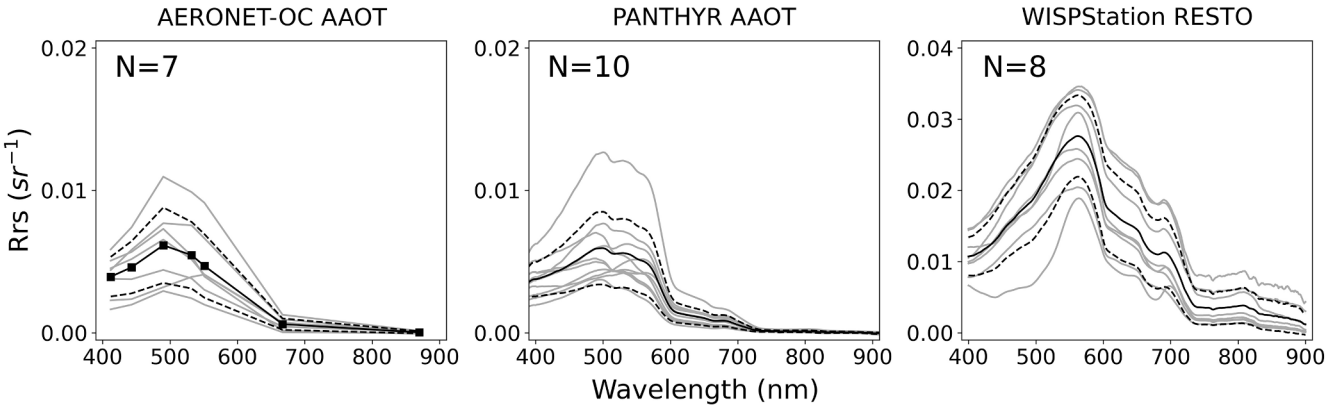

Fig. 3. *In situ* Rrs spectra, measured by autonomous multi- and hyperspectral radiometer systems, used for the match-up analysis of AAOT (AERONET-OC and PANTHYR) and RESTO (WISPStation). The thick black lines indicate mean values, the dashed lines indicate ± 1 standard deviation and the grey lines are all matched data with PRISMA. N represents the number of match-up spectra for the various instruments at each region. Note the different y-axis scale used for WISPStation RESTO.

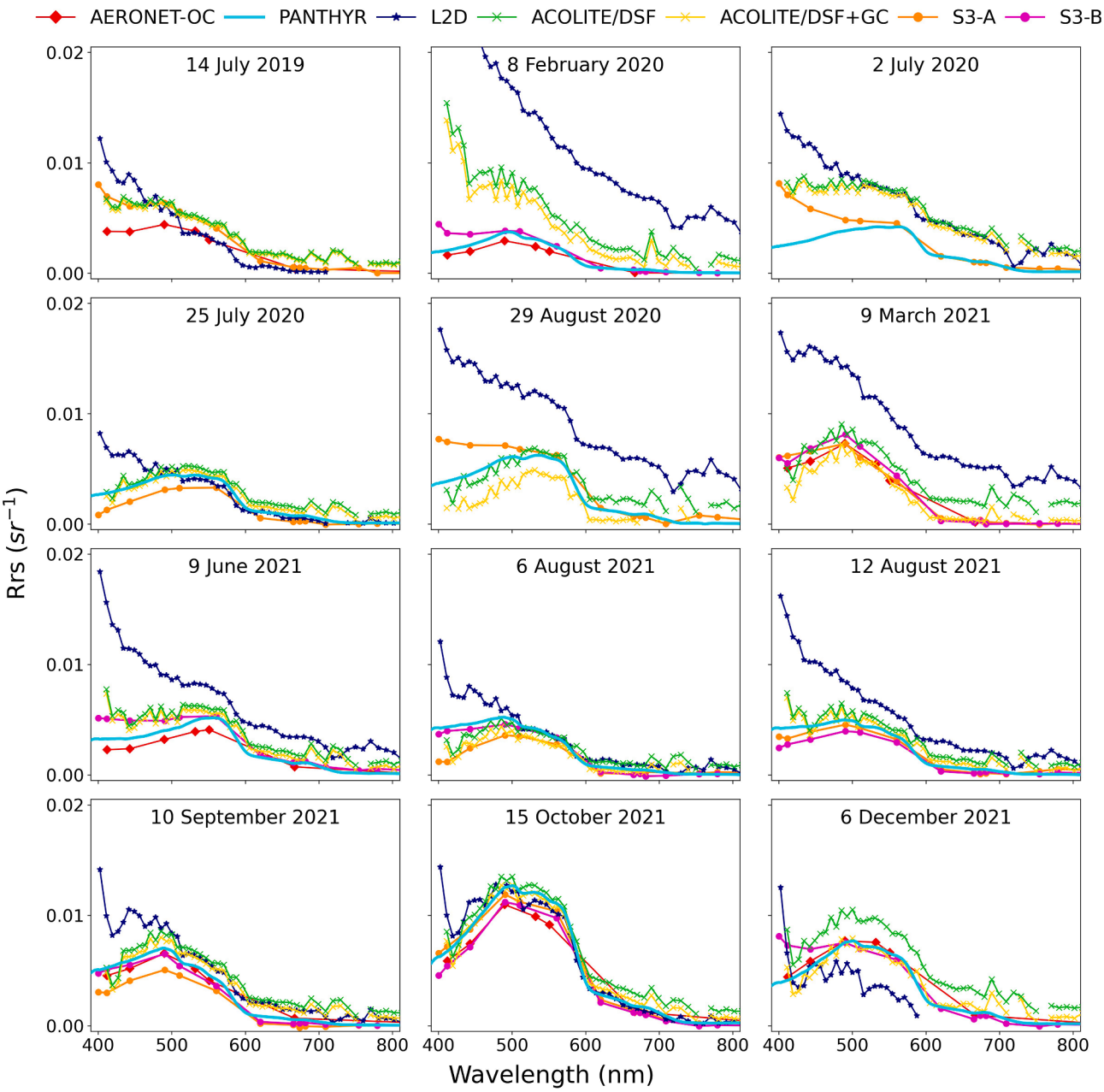

Fig. 4. Qualitative comparison of Remote sensing reflectance at AAOT site. *In situ* Rrs obtained from autonomous radiometer systems: AERONET-OC (red) and PANTHYR (cyan). PRISMA Rrs processed using: Level 2 standard atmospheric correction processor (L2D) (blue); ACOLITE atmospheric correction tool with the dark spectrum fitting (DSF) algorithm (ACOLITE/DSF) (green) and with the addition of sun-glint correction (ACOLITE/DSF + GC) (yellow); Sentinel-3A and B OLCI Rrs retrieved as baseline water products: respectively S3-A (orange) and S3-B (magenta). (For interpretation of the references to color in this figure legend, the reader is referred to the web version of this article.)

sites, respectively. The main purpose of the qualitative comparison is to showcase for each date the different match-ups included in the analysis and to point out artefacts that may characterise either satellite or *in situ* data. As seen for FRMs in Fig. 3, there is a significant variability in magnitude and spectral shape between the two sites and among the dates. At AAOT, the Rrs spectra mostly had values<0.01 sr^{-1} (Fig. 4). Both *in situ* and satellite-derived Rrs raised and even doubled only on October 15, 2021, most likely due to the presence of a relatively high concentration of suspended sediments in the coastal zone of North Adriatic Sea. The deviation of L2D spectra with respect to FRMs at AAOT was remarkable on some dates, while Rrs derived from ACOLITE matched quite well with both FRMs and S3/OLCI. The plot on February 8, 2020 is a representative example, where the L2D spectrum is three times higher than PANTHYR, AERONET-OC and S3/OLCI and twice ACOLITE. This likely resulted from the values of AOT used in the atmospheric correction inversion, that are 0.137 in the L2D processor and 0.3131 in ACOLITE, while *in situ* measures 0.2618. The retrievals of aerosol properties in L2D processor and in ACOLITE are based on different approaches and the values of AOT differ, as reported in Supplementary Material 1 (see Supplementary Table 1 and Supplementary Fig. 1). For instance, at AAOT, the L2D AOT values were equal to 0.137 for autumn–winter and 0.148 for spring-summer likely due to the lack of DDV in the scenes. L2D was therefore unable to represent the atmospheric condition during the PRISMA overpass. In general, if the used value of AOT is lower than the actual AOT, L2D results are higher than the other spectra; and if the used AOT is higher than the actual AOT, L2D results are lower than the FRMs and S3/OLCI data. On September 10, 2021 a good match between L2D and the other measurements

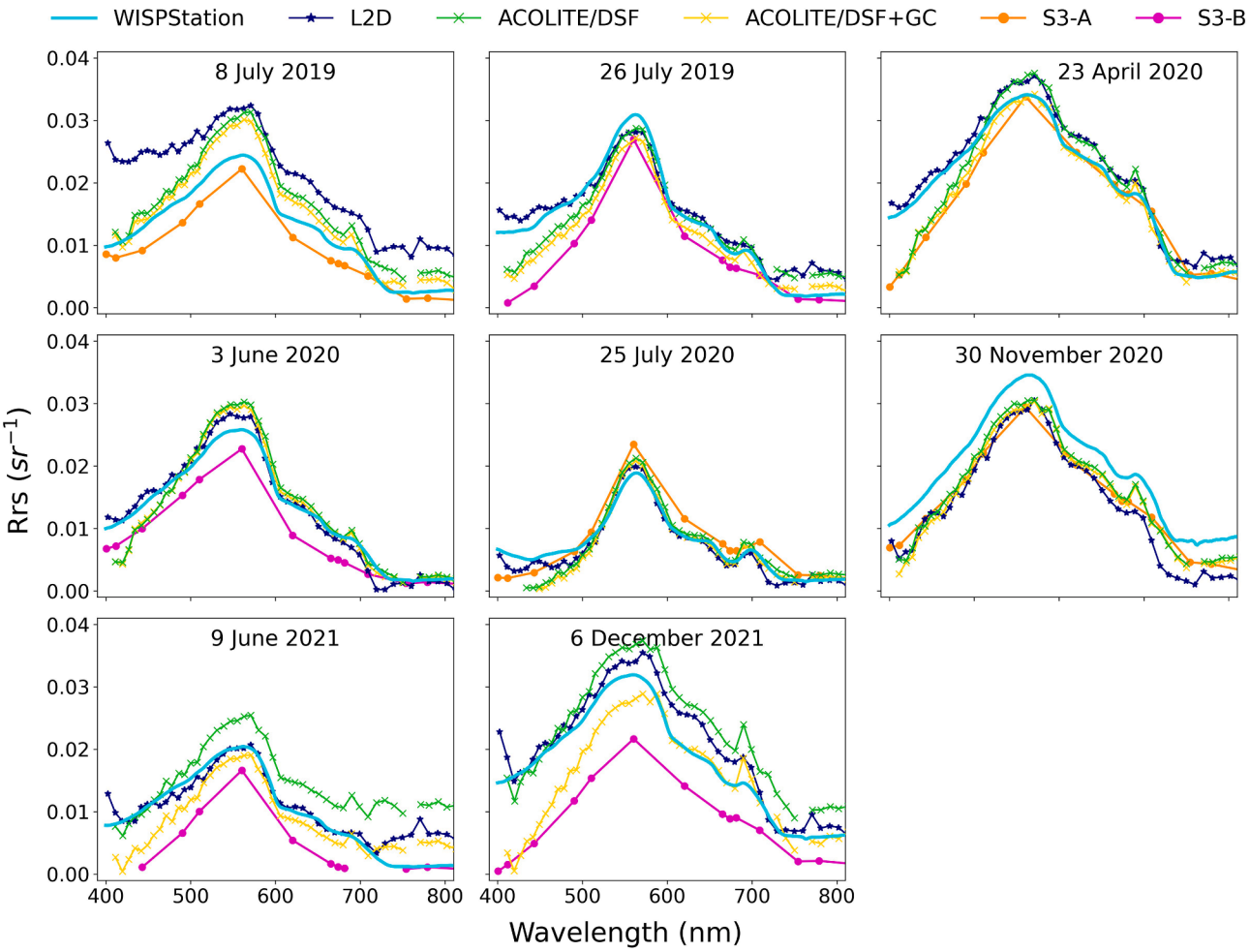

Fig. 5. Qualitative comparison of Remote sensing reflectance at RESTO. *In situ* Rrs obtained from autonomous hyperspectral radiometer WISPStation (cyan). PRISMA Rrs processed using: Level 2 standard atmospheric correction processor (L2D) (blue); ACOLITE atmospheric correction tool with the dark spectrum fitting (DSF) algorithm (ACOLITE/DSF) (green) and with the addition of sun-glint correction (ACOLITE/DSF + GC) (yellow); Sentinel-3A and B OLCI Rrs retrieved as baseline water products: respectively S3-A (orange) and S3-B (magenta). (For interpretation of the references to color in this figure legend, the reader is referred to the web version of this article.)

(excluding the blue spectral region) was found, since there is a good correspondence between the used and measured AOT. In Fig. 5, *in situ* and satellite spectra of RESTO are consistent, indicating a fair qualitative agreement. Large relative differences in magnitude among the spectra are not observed, as was the case for AAOT, except the lower values of ACOLITE with respect to FRMs in the range of 400–470 nm. In both *in situ* and satellite data, specific features of Chl-a and secondary pigments absorption can be observed during the summer, clearly visible on July 25, 2020. Moreover, remarkable are the high reflectance values characterising some dates and caused by high water turbidity (e.g. April 23, 2020). Still, striking is the presence of overestimated Rrs in the range of 400–500 nm affecting the whole L2D dataset at AAOT and only in a few cases at RESTO (e.g. June 8, 2019). These uncertainties could be due to the inaccurate estimation of AOT or the aerosol model used in the atmospheric correction procedure. As stated in Warren et al. (2019), land-based atmospheric correction processors like L2D showed improved performance in inland waters, because there are many more land pixels available to calculate a better estimate of AOT. This suggests that the L2D processor is better suited to correct inland water bodies rather than coastal zones. Overall, inaccurate AOT values have larger impacts at AAOT than at RESTO, since errors on the estimated atmospheric reflectance represent a larger fraction of the low water reflectance measured at AAOT (e.g. Fig. 3). Another issue that could affect the match-ups is the effect of sun-glint on Rrs, which is corrected in ACOLITE/DSF + GC spectra, but it can still impact ACOLITE/DSF and L2D data, as likely on July 8, 2019 at RESTO and March 9, 2021 at AAOT. On these dates, L2D spectra increased by a factor of 0.5 or more due to sun-glint, although they looked very similar in shape to the other spectra.

While the *in situ* measured water spectra are rather smooth, the PRISMA data from both L2D and ACOLITE show band-to-band spectral variations, especially in the 400–560 nm region. These spectral jumps are likely the result of inter-band calibration issues (see e.g. Lavigne and Ruddick, 2021). L2D also shows a spectral feature near the oxygen absorption feature at 762 nm, which is not output by ACOLITE due to the gas transmittance threshold (Section 3.4.2).

Quantitative comparisons between PRISMA reflectances and *in situ* hyperspectral data (spectrally resampled to the FWHM of PRISMA bands) are presented in Fig. 6 with a single scatterplot for L2D and ACOLITE (DSF and DSF + GC) Rrs at each site. Following our observations in the qualitative analysis, the match-up comparison depicted different results for the two sites with the best performances at RESTO for both L2D and ACOLITE data. At AAOT, ACOLITE showed better correlation with PANTHYR data, returning lower uncertainties and bias than L2D. ACOLITE/DSF + GC performed similarly to ACOLITE/DSF but with lower RMSD, MAD and MAPD. In the blue and red spectral regions, L2D reflectance is significantly larger than the PANTHYR data, with only sparse points near or under the 1:1 line. ACOLITE likewise shows a

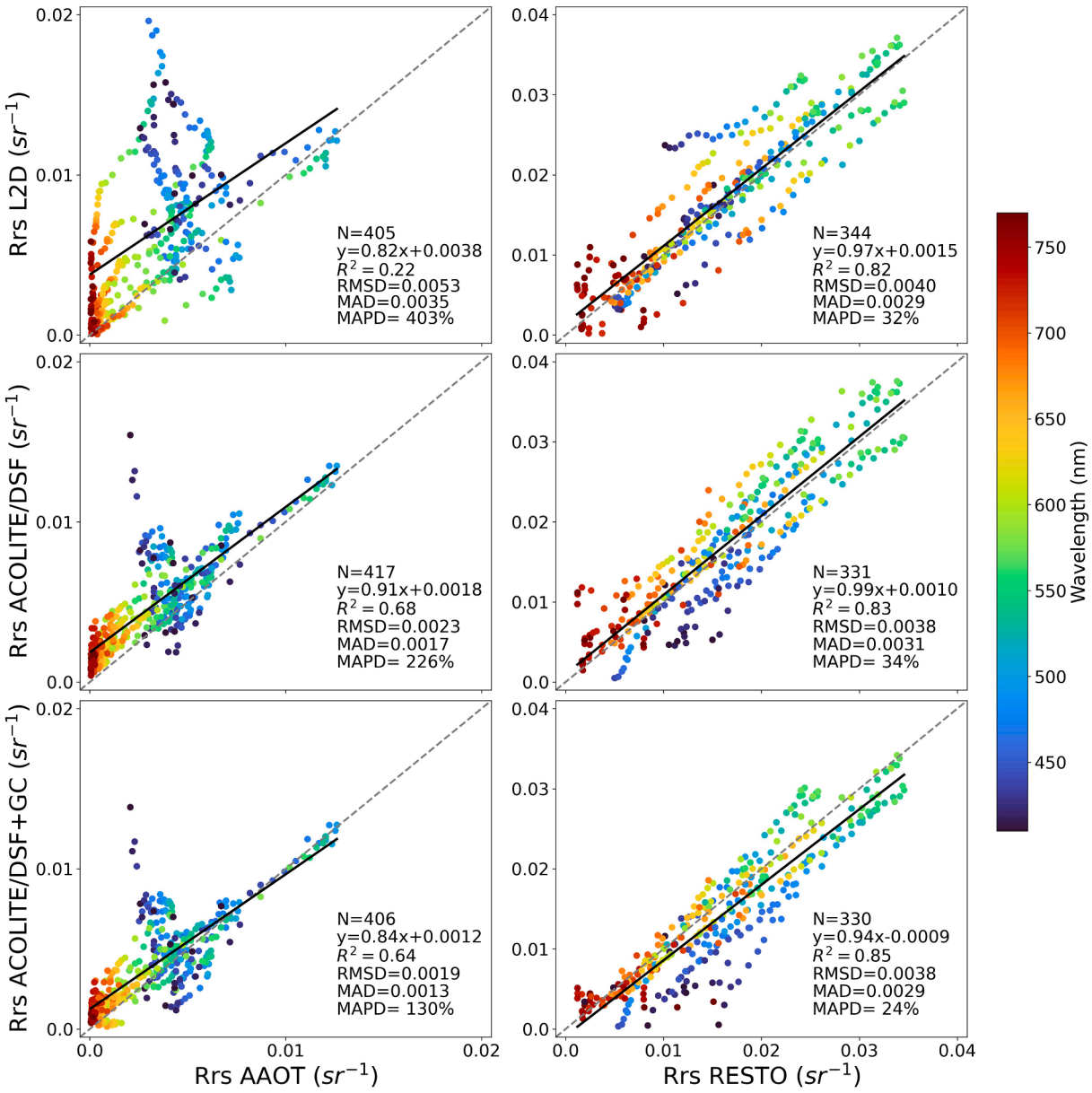

Fig. 6. Scatterplots of *in situ* Rrs from AAOT (plots on the left) and RESTO (plots on the right) versus PRISMA Rrs processed using: Level 2 standard atmospheric correction processor (L2D) (top), ACOLITE atmospheric correction tool with the dark spectrum fitting (DSF) algorithm (ACOLITE/DSF) (middle) and with the addition of sun-glint correction (ACOLITE/DSF + GC) (bottom) for the 410–770 nm spectral range. Black solid line is the best-fit linear regression. Grey dashed line is the 1:1 line. Note the different axis scales used for RESTO plots.

larger range of Rrs retrieved for bands < 450 nm, reflecting the challenging estimation of atmospheric path reflectance in the blue spectral region for the offshore clear waters of northern Adriatic Sea. For RESTO, both L2D and ACOLITE showed closer correlation ($R^2 > 0.81$) and lower MAPD, while RMSD and MAD were higher compared to ACOLITE at AAOT, likely because the points of the scatterplots were more scattered and distributed almost in parallel to the best-fit linear regression and to the 1:1 line. In particular, for L2D, the two spectra acquired on July 8, 2019 and November 30, 2020 show a significant over/underestimation of *in situ* Rrs, respectively, as evident in Fig. 5. The shift of the whole spectrum down/up, with a spectrally rather constant factor, is probably due to erroneous aerosol parametrization in the L2D atmospheric correction module or to glint presence. At RESTO, noticeable is the underestimation of the blue points (approximately in the range 410–480 nm) in ACOLITE, as a result of the difficult atmospheric correction in this spectral range. Overall, Fig. 6 indicates that the low water-leaving signal at AAOT is more sensitive to the atmospheric correction in the blue and the NIR spectral regions. Notably, L2D shows worse performance for the lower reflectance offshore waters than for the turbid and productive waters of Trasimeno Lake.

The distribution of SA provides a quantitative evaluation of the spectral similarity of FRMs and PRISMA-derived Rrs in terms of shape, where a smaller SA indicates a more similar shape. The SA was calculated for all the match-ups for each site and for the three atmospheric correction algorithms in the 410–770 nm range (Fig. 7) to assess the capability of reproducing the spectral shape of *in situ* data, that would enable the retrieval of specific features (i.e. absorption peaks of Chl-a and secondary pigments). Overall, larger SA are retrieved at AAOT than at RESTO, indicating a more difficult atmospheric correction process for the former, likely impacted by the lower target Rrs. At AAOT, the SA of ACOLITE/DSF + GC was better aligned with the SA measured by PANTHYR than that of L2D, having a tighter distribution and the lowest median of spectral angle (11.5° *vs* 19.5°), suggesting that ACOLITE with the glint correction best reproduced the spectral shape of *in*

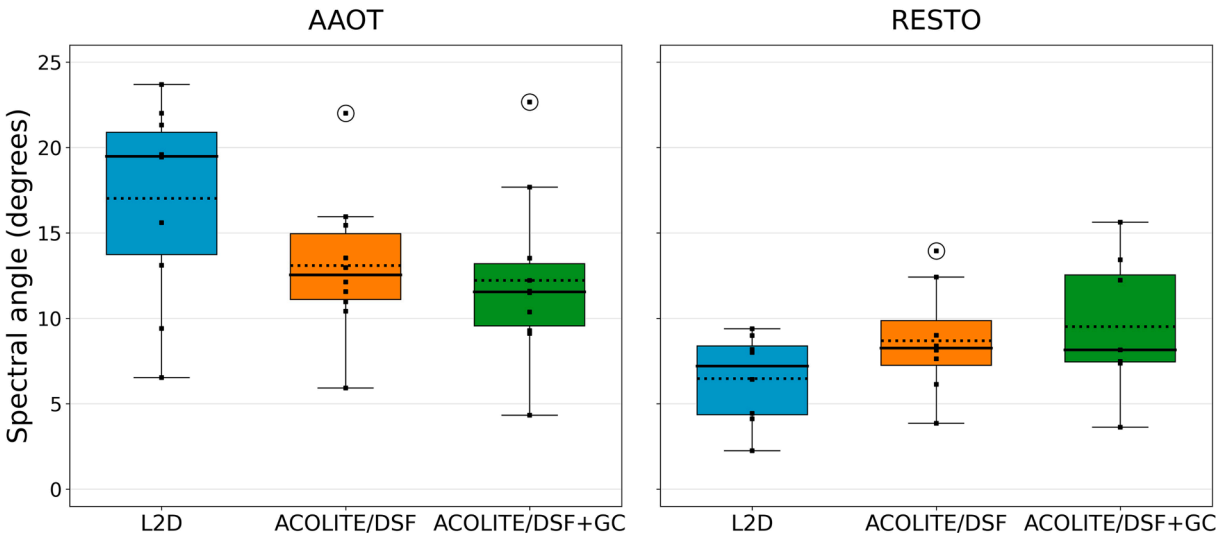

Fig. 7. Box plots of spectral angle for AAOT (left) and RESTO (right) derived by comparing FRMs to PRISMA Rrs processed using: Level 2 standard atmospheric correction processor (L2D) (cyan), ACOLITE atmospheric correction tool with the dark spectrum fitting (DSF) algorithm (ACOLITE/DSF) (orange) and with the addition of sun-glint correction (ACOLITE/DSF + GC) (green) in the 410–770 nm spectral range. This is a measure of similarity of the corrected PRISMA and *in situ* spectra and a smaller angle suggests a more similar shape. Black solid line shows the median, black dotted line is the mean value, box limits indicate the 25th and 75th percentiles, whiskers extend 1.5 times the interquartile range. Black squares in the plots represent the value of spectral angle for each match-up. Circled squares depict the outliers. (For interpretation of the references to color in this figure legend, the reader is referred to the web version of this article.)

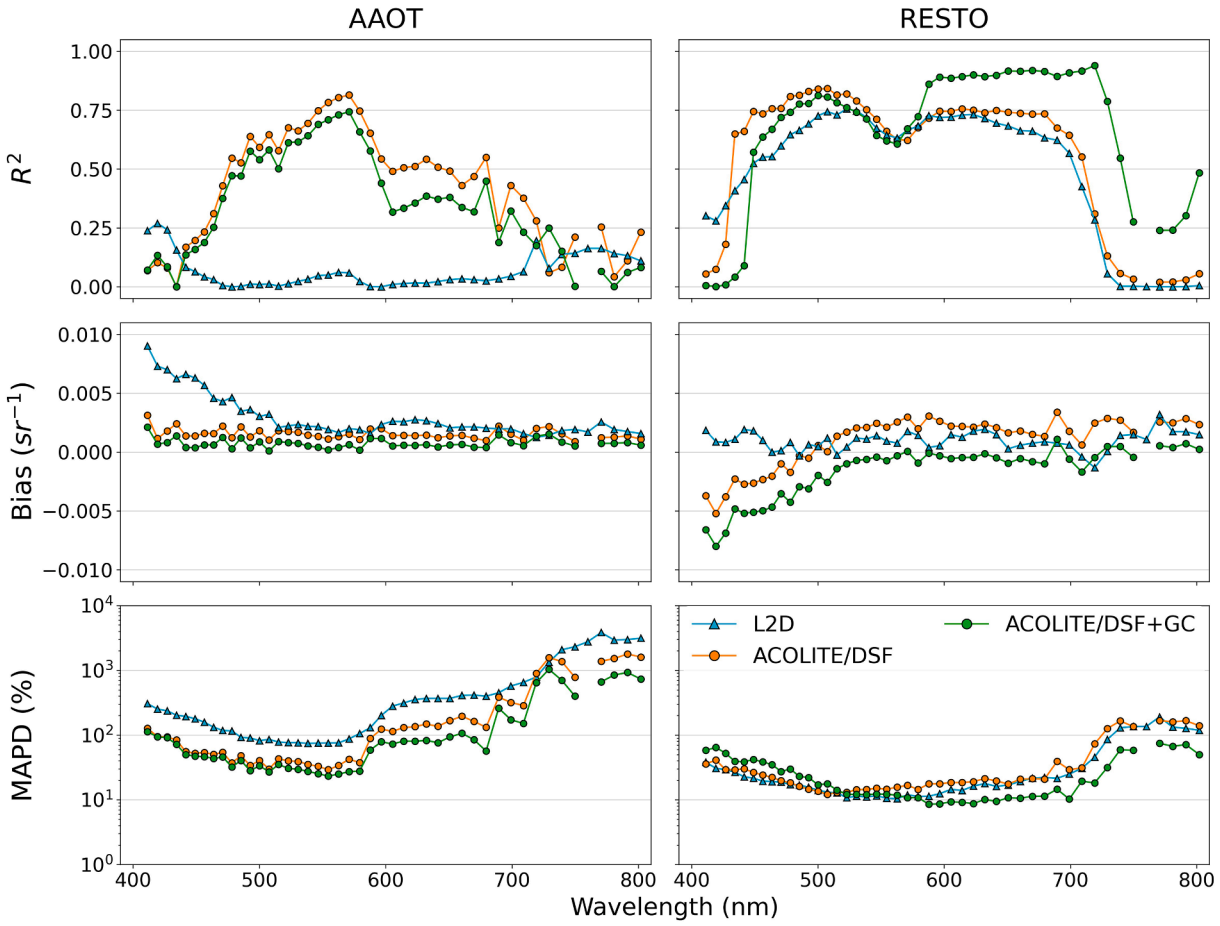

Fig. 8. Plots of the spectral statistics for AAOT and RESTO match-ups. PRISMA Rrs processed using: Level 2 standard atmospheric correction processor (L2D) (cyan), ACOLITE atmospheric correction tool with the dark spectrum fitting (DSF) algorithm (ACOLITE/DSF) (orange) and with the addition of sun-glint correction (ACOLITE/DSF + GC) (green). R^2 is the coefficient of determination (square of the Pearson product correlation), Bias is the averaged difference between *in situ* and PRISMA values and MAPD is the Mean Absolute Percentage Difference. The plots of MAPD are shown on a log scale. (For interpretation of the references to color in this figure legend, the reader is referred to the web version of this article.)

situ data in coastal water. At RESTO, the medians had similar values (8.2°-8.1° *vs* 7.2°), but L2D achieved the lowest median and interquartile ranges of SA with values<8°. The larger range retrieved by ACOLITE/DSF + GC compared to ACOLITE/DSF indicates that the glint correction may incorrectly attribute some of the residual SWIR reflectance (e.g. from land adjacency) to the air–water interface reflectance. The better performance of L2D in inland water implies that the derived spectra are more similar in shape to the *in situ* data, improving the retrieval of Chl-a and secondary pigments absorption properties.

Descriptive statistics and error metrics are reported spectrally for each atmospheric correction algorithm versus FRMs, calculated for AAOT and RESTO (Fig. 8). At AAOT, both ACOLITE and L2D performed poorly and overestimated Rrs. ACOLITE gave the best performance in the range between 470 and 580 nm ($R^2 > 0.5$, Bias < 0.0015 and MAPD $< 35\%$), where the observed reflectance was highest. ACOLITE/DSF and ACOLITE/DSF + GC had a very similar behaviour, with higher R^2 for the former and slightly lower errors (Bias and MAPD) for the latter. Bias had a flat trend for ACOLITE, with a gradual increase towards the shorter wavelength bands for L2D, which could be associated with the larger divergence seen in the spectra in Fig. 4 and in the scatter plot in Fig. 6, likely due to the methodology used by the L2D processor to estimate the AOT. Values of MAPD higher than 100% in the Red and NIR spectral region were likely due to the very low water-leaving signal and high water absorption, so the absolute differences turned into very large relative differences. Furthermore, lower SNR of PRISMA L1 at these wavelengths (see Fig. 2) can even yield higher uncertainties as observable either at AAOT and at RESTO.

Both L2D and ACOLITE at RESTO had the highest R^2, with values >0.5 for all the bands in the ranges of 460–700 nm and 460–740 nm, respectively. For ACOLITE, Bias (in terms of absolute value) decreased from the Blue to the NIR, consistent with higher influence of atmospheric signals in the shorter wavelength bands. Negative Bias in the Blue range indicated a tendency to overcorrect for atmospheric effects. For L2D, Bias is fairly uniform across the full spectrum. RESTO returned the lowest MAPD with values <25% in the Green and Red bands (between 500 and 680 nm, i.e. in the bands with the highest observed reflectance), a slight rise of relative differences to the Blue (high atmospheric signal), which was more pronounced in ACOLITE, and a marked increase for the NIR (low water-leaving signal plus low SNR).

5. Conclusions

This work presented the assessment of water reflectance derived from the PRISMA hyperspectral sensor in inland and coastal waters characterised by different optical properties. Above-water *in situ* reflectance from autonomous hyper- and multispectral radiometer systems were used to evaluate PRISMA L2D products distributed by the Italian Space Agency and Rrs data derived from the atmospheric correction tool ACOLITE, adapted for processing PRISMA Level 1 products. A marked difference was observed in the performance at the coastal AAOT and the lacustrine RESTO sites: both L2D and ACOLITE performed adequately in inland waters, while ACOLITE showed better results compared to L2D in coastal waters. The land-based atmospheric correction processor, i.e. L2D, showed satisfactory performance in inland waters, as several land pixels are available to estimate AOT. On the contrary, the lack of land pixels in the coastal site led to the selection of the AOT default values in the L2D processing, thus introducing errors on the estimated atmospheric reflectance that represent a larger fraction of the low water reflectance measured at AAOT. This suggests that the L2D processor is better suited to correct inland water bodies rather than coastal zones. On the other hand, ACOLITE was primarily designed for processing multispectral images for aquatic remote sensing applications and it was here modified for processing of PRISMA. ACOLITE performed satisfactorily at AAOT with a more accurate estimation of AOT and a further improvement given by the correction of sun-glint, taking advantage of the available processing options tailored for aquatic environments. The PRISMA SNR analysis demonstrated that SNR remained significantly below the radiometric requirements recommended for current ocean colour missions and/or future imaging spectrometers, although a spatial aggregation to 60 or 90 m aiming to improve the SNR may be required for specific aquatic applications.

Overall, the results over these water bodies are encouraging, confirming the consistency of PRISMA Rrs and its capability in providing adequate radiometric products. Nevertheless, the match-up analysis presented in this study is limited to two sites, thus it cannot be exhaustive because it represents a quite limited range of water optical properties. Further studies are needed to confirm our results and extend performance analysis to other water bodies, characterised by different optical water types. The availability of FRMs from autonomous hyperspectral radiometers is fundamental to provide validation data and thoroughly assess the radiometric performance of PRISMA Rrs for any spectral band between 400 and 900 nm.

PRISMA, as a precursory mission, represents an important step forward in spaceborne imaging spectroscopy, even if the observational capabilities in terms of regular acquisitions over a region of interest are sometimes suboptimal (Cogliati et al., 2021; Marshall et al., 2022). As demonstrated in Hestir et al. (2015), an archival and global mapping mission is needed to provide reliable, repeatable monitoring for ecosystem studies and to meet the data requirements of end-users. In the next few years, hyperspectral FRMs will be also required for the intercomparison and the synergistic exploitation of the current and expected imaging spectroscopy missions. Synergies with other hyperspectral sensors will improve the temporal observational capabilities of a single mission, meeting the monitoring needs of end-users (Guanter et al., 2019; Taramelli et al., 2020). A more consistent dataset of PRISMA data frequently acquired in an increasing number of autonomous hyperspectral radiometers with global contributors will enable further analysis of the PRISMA performances over clear, turbid and productive waters. An increased number of match-ups, including satellite overpasses and measurement sites, will allow more robust statistical analyses, providing further information on the performance under varying observation geometry, atmospheric conditions and across various optical water types. Moreover, the recent launch of EnMAP and the expected hyperspectral missions are boosting the development and the improvement of atmospheric correction processors adapted to hyperspectral sensors and specific for aquatic sites (i.e. POLYMER, SeaDAS, iCOR, etc.) thus exploiting a thorough evaluation of the different radiative transfer approaches as recently performed for multispectral sensors (Pahlevan et al., 2021b).

Declaration of Competing Interest

The authors declare that they have no known competing financial interests or personal relationships that could have appeared to influence the work reported in this paper.

Acknowledgements

This study was carried out using PRISMA Products, © of the Italian Space Agency (ASI), delivered under an ASI License to use. This work was made possible by the funding support of the agreement ASI-CNR, n. 20195HH0 “Attività scientifica di CAL/VAL della missione PRISMA - PRISCAV” and the project ASI-CNR, n. 2022-15-U.0 “PRISMA Products AND Applications for inland and coastal WATER - PANDA-WATER”. This work was also carried out in the context of the HYPERNETS (Grant agreement n° 775983), CERTO (Grant agreement n° 870349), PrimeWater (Grant agreement n° 870497) and Water-ForCE (Grant agreement n° 101004186) projects funded by the European Union’s Horizon 2020 research and innovation programme. The authors are grateful to Giuseppe Zibordi, Principal Investigator of the AAOT AERONET and AERONET-OC site for the maintenance and distribution of data to the community. ESA is acknowledged for funding the processing of the

PANTHYR data by WATERHYPERNET. Dieter Vansteenwegen, Matthew Beck and Kevin Ruddick are thanked for PANTHYR installation and support. The authors would like to thank the reviewers for their relevant comments and suggestions that helped to improve the previous version of the manuscript.

Appendix A. Supplementary material

Supplementary data to this article can be found online at https://doi.org/10.1016/j.isprsjprs.2022.08.009.

References

Antoine, D., Morel, A., 1999. A multiple scattering algorithm for atmospheric correction of remotely sensed ocean colour (MERIS instrument): principle and implementation for atmospheres carrying various aerosols including absorbing ones. Int. J. Remote Sens. 20 (9), 1875–1916. https://doi.org/10.1080/014311699212533.

ASI – Italian Space Agency, 2021. PRISMA Algorithm Theoretical Basis Document (ATBD), Issue 1, Date 14/12/2021. http://prisma.asi.it/missionselect/docs.php. (Accessed 7 May, 2022.

Bailey, S.W., Werdell, P.J., 2006. A multi-sensor approach for the on-orbit validation of ocean color satellite data products. Remote Sens. Environ. 102 (1–2), 12–23. https://doi.org/10.1016/j.rse.2006.01.015.

Barnsley, M.J., Settle, J.J., Cutter, M.A., Lobb, D.R., Teston, F., 2004. The PROBA/CHRIS mission: A low-cost smallsat for hyperspectral multiangle observations of the earth surface and atmosphere. IEEE Trans. Geosci. Remote Sens. 42 (7), 1512–1520. https://doi.org/10.1109/TGRS.2004.827260.

Bassani, C., Manzo, C., Braga, F., Bresciani, M., Giardino, C., Alberotanza, L., 2015. The impact of the microphysical properties of aerosol on the atmospheric correction of hyperspectral data in coastal waters. Atmos. Meas. Tech. 8 (3), 1593–1604. https://doi.org/10.5194/amt-8-1593-2015.

Berthon, J.F., Zibordi, G., 2004. Bio-optical relationships for the northern Adriatic Sea. Int. J. Remote Sens. 25 (7–8), 1527–1532. https://doi.org/10.1080/01431160310001592544.

Bracaglia, M., Volpe, G., Colella, S., Santoleri, R., Braga, F., Brando, V.E., 2019. Using overlapping VIIRS scenes to observe short term variations in particulate matter in the coastal environment. Remote Sens. Environ. 233, 111367. https://doi.org/10.1016/j.rse.2019.111367.

Bracaglia, M., Santoleri, R., Volpe, G., Colella, S., Benincasa, M., Brando, V.E., 2020. A virtual geostationary ocean color sensor to analyze the coastal optical variability. Remote Sens. 12 (10), 1539. https://doi.org/10.3390/rs12101539.

Braga, F., Giardino, C., Bassani, C., Matta, E., Candiani, G., Strömbeck, N., Adamo, M., Bresciani, M., 2013. Assessing water quality in the northern Adriatic Sea from HICO™ data. Remote Sens. Lett. 4 (10), 1028–1037. https://doi.org/10.1080/2150704X.2013.830203.

Brando, V.E., Dekker, A.G., 2003. Satellite hyperspectral remote sensing for estimating estuarine and coastal water quality. IEEE Trans. Geosci. Remote Sens. 41 (6), 1378–1387. https://doi.org/10.1109/TGRS.2003.812907.

Brando, V.E., Lovell, J.L., King, E.A., Boadle, D., Scott, R., Schroeder, T., 2016. The potential of autonomous ship-borne hyperspectral radiometers for the validation of ocean color radiometry data. Remote Sensing 8 (2), 150. https://doi.org/10.3390/rs8020150.

Bresciani, M., Pinardi, M., Free, G., Luciani, G., Ghebrehiwot, S., Laanen, M., Peters, S., Della Bella, V., Padula, R., Giardino, C., 2020. The use of multisource optical sensors to study phytoplankton spatio-temporal variation in a Shallow Turbid Lake. Water 12 (1), 284. https://doi.org/10.3390/w12010284.

Bresciani, M., Giardino, C., Fabbretto, A., Pellegrino, A., Mangano, S., Free, G., Pinardi, M., 2022. Application of New Hyperspectral Sensors in the Remote Sensing of Aquatic Ecosystem Health: Exploiting PRISMA and DESIS for Four Italian Lakes. Resources 11 (2), 8. https://doi.org/10.3390/resources11020008.

Cavaleri, L., 2000. The oceanographic tower Acqua Alta—activity and prediction of sea states at Venice. Coast. Eng. 39 (1), 29–70. https://doi.org/10.1016/S0378-3839(99)00053-8.

Cawse-Nicholson, K., Townsend, P.A., Schimel, D., Assiri, A.M., Blake, P.L., Buongiorno, M.F., Campbell, P., Carmon, N., Casey, K.A., Correa-Pabón, R.E., Dahlin, K.M., Dashti, H., Dennison, P.E., Dierssen, H., Erickson, A., Fisher, J.B., Frouin, R., Gatebe, C.K., Gholizadeh, H., Gierach, M., Glenn, N.F., Goodman, J.A., Griffith, D.M., Guild, L., Hakkenberg, C.R., Hochberg, E.J., Holmes, T.R.H., Hu, C., Hulley, G., Huemmrich, K.F., Kudela, R.M., Kokaly, R.F., Lee, C.M., Martin, R., Miller, C.E., Moses, W.J., Muller-Karger, F.E., Ortiz, J.D., Otis, D.B., Pahlevan, N., Painter, T.H., Pavlick, R., Poulter, B., Qi, Y.i., Realmuto, V.J., Roberts, D., Schaepman, M.E., Schneider, F.D., Schwandner, F.M., Serbin, S.P., Shiklomanov, A. N., Stavros, E.N., Thompson, D.R., Torres-Perez, J.L., Turpie, K.R., Tzortziou, M., Ustin, S., Yu, Q., Yusup, Y., Zhang, Q., 2021. NASA's surface biology and geology designated observable: A perspective on surface imaging algorithms. Remote Sens. Environ. 257, 112349.

Cazzaniga, I., Zibordi, G., Mélin, F., Kwiatkowska, E., Talone, M., Dessailly, D., Gossn, J. I., Müller, D., 2022. Evaluation of OLCI Neural Network Radiometric Water Products. IEEE Geosci. Remote Sens. Lett. 19, 1–5. https://doi.org/10.1109/LGRS.2021.3136291.

Chami, M., Lafrance, B., Fougnie, B., Chowdhary, J., Harmel, T., Waquet, F., 2015. OSOAA: a vector radiative transfer model of coupled atmosphere-ocean system for a rough sea surface application to the estimates of the directional variations of the water leaving reflectance to better process multi-angular satellite sensors data over the ocean. Opt. Express 23 (21), 27829–27852. https://doi.org/10.1364/OE.23.027829.

Cogliati, S., Sarti, F., Chiarantini, L., Cosi, M., Lorusso, R., Lopinto, E., Miglietta, F., Genesio, L., Guanter, L., Damm, A., Pérez-López, S., Scheffler, D., Tagliabue, G., Panigada, C., Rascher, U., Dowling, T.P.F., Giardino, C., Colombo, R., 2021. The PRISMA imaging spectroscopy mission: overview and first performance analysis. Remote Sens. Environ. 262, 112499.

Concha, J.A., Bracaglia, M., Brando, V.E., 2021. Assessing the influence of different validation protocols on Ocean Colour match-up analyses. Remote Sens. Environ. 259, 112415. https://doi.org/10.1016/j.rse.2021.112415.

Coppo, P., Brandani, F., Faraci, M., Sarti, F., Dami, M., Chiarantini, L., Ponticelli, B., Giunti, L., Fossati, E., Cosi, M., 2020. Leonardo spaceborne infrared payloads for Earth observation: SLSTRs for Copernicus Sentinel 3 and PRISMA hyperspectral camera for PRISMA satellite. Appl. Opt. 59 (23), 6888–6901. https://doi.org/10.1364/AO.389485.

Dierssen, H.M., Ackleson, S.G., Joyce, K.E., Hestir, E.L., Castagna, A., Lavender, S., McManus, M.A., 2021. Living up to the hype of hyperspectral aquatic remote sensing: science, resources and outlook. Front. environ. sci. 9 https://doi.org/10.3389/fenvs.2021.649528.

Dierssen, H., McManus, G.B., Chlus, A., Qiu, D., Gao, B.C., Lin, S., 2015. Space station image captures a red tide ciliate bloom at high spectral and spatial resolution. Proc. Natl. Acad. Sci. 112 (48), 14783–14787. https://doi.org/10.1073/pnas.1512538112.

Donlon, C.J., Zibordi, G., 2014. In Situ Optical Radiometry. In: Zibordi, G., Donlon, C.J., Parr, A.C. (Eds.), Experimental Methods in the Physical Sciences, vol. 47. Academic Press, pp. 245–246.

Esposito, M., Marchi, A.Z., 2019. In-orbit demonstration of the first hyperspectral imager for nanosatellites. In International Conference on Space Optics—ICSO 2018 (Vol. 11180, p. 1118020). International Society for Optics and Photonics. https://doi.org/10.1117/12.2535991.

Feingersh, T., Ben-Dor, E., 2015. Shalom–a commercial hyperspectral space mission. Opt. Payloads Space Missions 247–263.

Formaro, R., Longo, F., Varacalli, G., Fasano, L., Pulcino, V., 2021. ASI roadmap in technology and programmes for earth advanced monitoring and assessment of hazards. In: 2021 IEEE International Geoscience and Remote Sensing Symposium IGARSS. IEEE. pp. 1875–1878. https://doi.org/10.1109/IGARSS47720.2021.9554834.

Free, G., Bresciani, M., Pinardi, M., Giardino, C., Alikas, K., Kangro, K., Rõõm, E.-I., Vaičiūtė, D., Bučas, M., Tiškus, E., Hommersom, A., Laanen, M., Peters, S., 2021. Detecting climate driven changes in chlorophyll-a using high frequency monitoring: the impact of the 2019 European Heatwave in Three Contrasting Aquatic Systems. Sensors 21 (18), 6242.

Free, G., Bresciani, M., Pinardi, M., Peters, S., Laanen, M., Padula, R., Cingolani, A., Charavgis, F., Giardino, C., 2022. Shorter blooms expected with longer warm periods under climate change: an example from a shallow meso-eutrophic Mediterranean lake. Hydrobiologia 1–16. https://doi.org/10.1007/s10750-021-04773-w.

Frouin, R.J., Franz, B.A., Ibrahim, A., Knobelspiesse, K., Ahmad, Z., Cairns, B., Chowdhary, J., Dierssen, H.M., Tan, J., Dubovik, O., Huang, X., Davis, A.B., Kalashnikova, O., Thompson, D.R., Remer, L.A., Boss, E., Coddington, O., Deschamps, P.-Y., Gao, B.-C., Gross, L., Hasekamp, O., Omar, A., Pelletier, B., Ramon, D., Steinmetz, F., Zhai, P.-W., 2019. Atmospheric correction of satellite ocean-color imagery during the PACE era. Front. Earth Sci. 7 https://doi.org/10.3389/feart.2019.00145.

Gao, B.C., Montes, M.J., Ahmad, Z., Davis, C.O., 2000. Atmospheric correction algorithm for hyperspectral remote sensing of ocean color from space. Appl Opt 39 (6), 887–896. https://doi.org/10.1364/AO.39.000887.

George, R., Padalia, H., Kushwaha, S.P.S., 2014. Forest tree species discrimination in western Himalaya using EO-1 Hyperion. Int. J. Appl. Earth Obs. Geoinf. 28, 140–149. https://doi.org/10.1016/j.jag.2013.11.011.

Giannini, F., Hunt, B.P., Jacoby, D., Costa, M., 2021. Performance of OLCI Sentinel-3A satellite in the Northeast Pacific coastal waters. Remote Sens. Environ. 256, 112317. https://doi.org/10.1016/j.rse.2021.112317.

Giardino, C., Brando, V.E., Dekker, A.G., Strömbeck, N., Candiani, G., 2007. Assessment of water quality in Lake Garda (Italy) using Hyperion. Remote Sens. Environ. 109 (2), 183–195. https://doi.org/10.1016/j.rse.2006.12.017.

Giardino, C., Brando, V.E., Gege, P., Pinnel, N., Hochberg, E., Knaeps, E., Reusen, I., Doerffer, R., Bresciani, M., Braga, F., Foerster, S., Champollion, N., Dekker, A., 2019. Imaging spectrometry of inland and coastal waters: state of the art, achievements and perspectives. Surv. Geophys. 40 (3), 401–429.

Giardino, C., Bresciani, M., Braga, F., Fabbretto, A., Ghirardi, N., Pepe, M., Gianinetto, M., Colombo, R., Cogliati, S., Ghebrehiwot, S., Laanen, M., Peters, S., Schroeder, T., Concha, J.A., Brando, V.E., 2020. First Evaluation of PRISMA Level 1 Data for Water Applications. Sensors 20 (16), 4553.

Giardino, C., Bresciani, M., Fabbretto, A., Ghirardi, N., Mangano, S., Pellegrino, A., Vaiciute, D., Braga, F. Brando., V.E., Laanen, M. et al., 2021. Hyperspectral Prisma Products of Aquatic Systems. In: 2021 IEEE International Geoscience and Remote Sensing Symposium IGARSS. IEEE. pp. 1229–1232. https://doi.org/10.1109/IGARSS47720.2021.9553761.

Goetz, A.F., 2009. Three decades of hyperspectral remote sensing of the Earth: A personal view. Remote Sens. Environ. 113, S5–S16. https://doi.org/10.1016/j.rse.2007.12.014.

Goetz, A.F., Vane, G., Solomon, J.E., Rock, B.N., 1985. Imaging spectrometry for earth remote sensing. Science 228 (4704), 1147–1153. https://doi.org/10.1126/science.228.4704.1147.

Gordon, H.R., 1978. Removal of atmospheric effects from satellite imagery of the oceans. Appl. Opt. 17 (10), 1631–1636. https://doi.org/10.1364/AO.17.001631.
Guanter, L., Estellés, V., Moreno, J., 2007. Spectral calibration and atmospheric correction of ultra-fine spectral and spatial resolution remote sensing data. Application to CASI-1500 data. Remote Sens. Environ. 109 (1), 54–65. https://doi.org/10.1016/j.rse.2006.12.005.
Guanter, L., Ruiz-Verdú, A., Odermatt, D., Giardino, C., Simis, S., Estellés, V., Heege, T., Dominguez-Gomez, J.A., Moreno, J., 2010. Atmospheric correction of ENVISAT/MERIS data over inland waters: Validation for European lakes. Remote Sens. Environ. 114 (3), 467–480. https://doi.org/10.1016/j.rse.2009.10.004.
Guanter, L., Kaufmann, H., Segl, K., Foerster, S., Rogass, C., Chabrillat, S., Kuester, T., Hollstein, A., Rossner, G., Chlebek, C., Straif, C., Fischer, S., Schrader, S., Storch, T., Heiden, U., Mueller, A., Bachmann, M., Mühle, H., Müller, R., Habermeyer, M., Ohndorf, A., Hill, J., Buddenbaum, H., Hostert, P., van der Linden, S., Leitão, P., Rabe, A., Doerffer, R., Krasemann, H., Xi, H., Mauser, W., Hank, T., Locherer, M., Rast, M., Staenz, K., Sang, B., 2015. The EnMAP spaceborne imaging spectroscopy mission for earth observation. Remote Sens. 7 (7), 8830–8857.
Guanter, L., Brell, M., Chan, J.C.W., Giardino, C., Gomez-Dans, J., Mielke, C., Morsdorf, F., Segl, K., Yokoya, N., 2019. Synergies of spaceborne imaging spectroscopy with other remote sensing approaches. Surv. Geophys. 40 (3), 657–687. https://doi.org/10.1007/s10712-018-9485-z.
Hestir, E.L., Brando, V.E., Bresciani, M., Giardino, C., Matta, E., Villa, P., Dekker, A.G., 2015. Measuring freshwater aquatic ecosystems: The need for a hyperspectral global mapping satellite mission. Remote Sens. Environ. 167, 181–195. https://doi.org/10.1016/j.rse.2015.05.023.
Holben, B.N., Eck, T.F., Slutsker, I., Tanré, D., Buis, J.P., Setzer, A., Vermote, E., Reagan, J.A., Kaufman, Y.J., Nakajima, T., Lavenu, F., Jankowiak, I., Smirnov, A., 1998. AERONET—A federated instrument network and data archive for aerosol characterization. Remote Sens. Environ. 66 (1), 1–16.
Holben, B.N., Tanré, D., Smirnov, A., Eck, T.F., Slutsker, I., Abuhassan, N., Newcomb, W. W., Schafer, J.S., Chatenet, B., Lavenu, F., Kaufman, Y.J., Castle, J.V., Setzer, A., Markham, B., Clark, D., Frouin, R., Halthore, R., Karneli, A., O'Neill, N.T., Pietras, C., Pinker, R.T., Voss, K., Zibordi, G., 2001. An emerging ground-based aerosol climatology: Aerosol optical depth from AERONET. J. Geophys. Res. Atmos. 106 (D11), 12067–12097.
Hu, C., Feng, L., Lee, Z., Davis, C.O., Mannino, A., McClain, C.R., Franz, B.A., 2012. Dynamic range and sensitivity requirements of satellite ocean color sensors: learning from the past. Appl. Opt. 51 (25), 6045–6062. https://doi.org/10.1364/AO.51.006045.
Ibrahim, A., Franz, B., Ahmad, Z., Healy, R., Knobelspiesse, K., Gao, B.C., Proctor, C., Zhai, P.W., 2018. Atmospheric correction for hyperspectral ocean color retrieval with application to the Hyperspectral Imager for the Coastal Ocean (HICO). Remote Sens. Environ. 204, 60–75. https://doi.org/10.1016/j.rse.2017.10.041.
Ilori, C.O., Pahlevan, N., Knudby, A., 2019. Analyzing performances of different atmospheric correction techniques for Landsat 8: application for coastal remote sensing. Remote Sens. 11 (4), 469. https://doi.org/10.3390/rs11040469.
IOCCG, 2000. Remote Sensing of Ocean Colour in Coastal, and Other Optically-Complex Waters, (ed. S. Sathyendranath). Dartmouth, NS, Canada, International Ocean-Colour Coordinating Group (IOCCG), 140pp. (Reports of the International Ocean-Colour Coordinating Group, No. 3) https://doi.org/10.25607/OBP-95.
Kaufman, Y.J., Tanré, D., Remer, L.A., Vermote, E.F., Chu, A., Holben, B.N., 1997. Operational remote sensing of tropospheric aerosol over land from EOS moderate resolution imaging spectroradiometer. J. Geophys. Res. Atmos. 102 (D14), 17051–17067. https://doi.org/10.1029/96JD03988.
Keith, D.J., Schaeffer, B.A., Lunetta, R.S., Gould Jr, R.W., Rocha, K., Cobb, D.J., 2014. Remote sensing of selected water-quality indicators with the hyperspectral imager for the coastal ocean (HICO) sensor. Int. J. Remote Sens. 35 (9), 2927–2962. https://doi.org/10.1080/01431161.2014.894663.
Krutz, D., Müller, R., Knodt, U., Günther, B., Walter, I., Sebastian, I., Säuberlich, T., Reulke, R., Carmona, E., Eckardt, A., et al., 2019. The instrument design of the DLR earth sensing imaging spectrometer (DESIS). Sensors 19 (7), 1622. https://doi.org/10.3390/s19071622.
Lavigne, H., Ruddick, K., 2021. Inter-band calibration for hyperspectral water remote sensing: demonstration for CHRIS-PROBA. In: 2021 IEEE International Geoscience and Remote Sensing Symposium IGARSS. IEEE. pp. 7771–7774. https://doi.org/10.1109/IGARSS47720.2021.9553637.
Lavigne, H., Vanhellemont, Q., Ruddick, K., Dogliotti, A., 2021. New processor and reference dataset for hyperspectral CHRIS-PROBA images over coastal and inland waters. In: 2021 IEEE International Geoscience and Remote Sensing Symposium IGARSS. IEEE. pp. 7916–7919. https://doi.org/10.1109/IGARSS47720.2021.9554430.
Liu, Y.-N., Zhang, J., Zhang, Y., Sun, W.-W., Jiao, L.-L., Sun, D.-X., Hu, X.-N., Ye, X., Li, Y.-D., Liu, S.-F., Cao, K.-Q., Chai, M.-Y., Zhou, W.-Y.-N., 2019. The advanced hyperspectral imager: aboard China's GaoFen-5 satellite. IEEE Geosci. Remote Sens. Mag. 7 (4), 23–32.
Loizzo, R., Guarini, R., Longo, F., Scopa, T., Formaro, R., Facchinetti, C., Varacalli, G., 2018. PRISMA: The Italian hyperspectral mission. In: IGARSS 2018-2018 IEEE International Geoscience and Remote Sensing Symposium. IEEE. pp. 175–178. https://doi.org/10.1109/IGARSS.2018.8518512.
Lu, B., Dao, P.D., Liu, J., He, Y., Shang, J., 2020. Recent advances of hyperspectral imaging technology and applications in agriculture. Remote Sens. 12 (16), 2659. https://doi.org/10.3390/rs12162659.
Lucke, R.L., Corson, M., McGlothlin, N.R., Butcher, S.D., Wood, D.L., Korwan, D.R., Li, R. R., Snyder, W.A., Davis, C.O., Chen, D.T., 2011. Hyperspectral Imager for the Coastal Ocean: instrument description and first images. Appl. Opt. 50 (11), 1501–1516. https://doi.org/10.1364/AO.50.001501.
Marshall, M., Belgiu, M., Boschetti, M., Pepe, M., Stein, A., Nelson, A., 2022. Field-level crop yield estimation with PRISMA and Sentinel-2. ISPRS J. Photogramm. Remote Sens. 187, 191–210.
Matsunaga, T., Iwasaki, A., Tsuchida, S., Iwao, K., Tanii, J., Kashimura, O., Nakamura, R., Yamamoto, H., Kato, S., et al., 2019. HISUI status toward 2020 launch. In: IGARSS 2019-2019 IEEE International Geoscience and Remote Sensing Symposium. IEEE. pp. 4495-4498. https://doi.org/10.1109/IGARSS.2019.8899179.
Mélin, F., Zibordi, G., Berthon, J.F., 2007. Assessment of satellite ocean color products at a coastal site. Remote Sens. Environ. 110 (2), 192–215.
Mobley, C.D., 1999. Estimation of the remote-sensing reflectance from above-surface measurements. Appl. Opt. 38 (36), 7442–7455.
Morel, A., Antoine, D., Gentili, B., 2002. Bidirectional reflectance of oceanic waters: accounting for Raman emission and varying particle scattering phase function. Appl. Opt. 41 (30), 6289–6306. https://doi.org/10.1364/AO.41.006289.
Moses, W.J., Bowles, J.H., Lucke, R.L., Corson, M.R., 2012. Impact of signal-to-noise ratio in a hyperspectral sensor on the accuracy of biophysical parameter estimation in case II waters. Opt. Express 20 (4), 4309–4330. https://doi.org/10.1364/OE.20.004309.
Moses, W.J., Gitelson, A.A., Berdnikov, S., Bowles, J.H., Povazhnyi, V., Saprygin, V., Wagner, E.J., Patterson, K.W., 2013. HICO-based NIR–red models for estimating chlorophyll-a concentration in productive coastal waters. IEEE Geosci. Remote Sens. Lett. 11 (6), 1111–1115. https://doi.org/10.1109/LGRS.2013.2287458.
Mouw, C.B., Greb, S., Aurin, D., DiGiacomo, P.M., Lee, Z., Twardowski, M., Binding, C., Hu, C., Ma, R., Moore, T., Moses, W., Craig, S.E., 2015. Aquatic color radiometry remote sensing of coastal and inland waters: Challenges and recommendations for future satellite missions. Remote Sens. Environ. 160, 15–30.
NASEM - National Academies of Sciences, Engineering, and Medicine, 2018. Thriving on our changing planet: A decadal strategy for Earth observation from space. Washington, DC. The National Academies Press. https://doi.org/10.17226/24938.
Niro, F., Goryl, P., Dransfeld, S., Boccia, V., Gascon, F., Adams, J., Themann, B., Scifoni, S., Doxani, G., 2021. European Space Agency (ESA) Calibration/Validation Strategy for Optical Land-Imaging Satellites and Pathway towards Interoperability. Remote Sens. 13 (15), 3003. https://doi.org/10.3390/rs13153003.
Niroumand-Jadidi, M., Bovolo, F., Bruzzone, L., 2020. Water quality retrieval from PRISMA Hyperspectral images: first experience in a turbid lake and comparison with Sentinel-2. Remote Sens. 12 (23), 3984. https://doi.org/10.3390/rs13122381.
Pahlevan, N., Sarkar, S., Franz, B.A., Balasubramanian, S.V., He, J., 2017. Sentinel-2 MultiSpectral Instrument (MSI) data processing for aquatic science applications: Demonstrations and validations. Remote Sens. Environ. 201, 47–56. https://doi.org/10.1016/j.rse.2017.08.033.
Pahlevan, N., Smith, B., Binding, C., Gurlin, D., Li, L., Bresciani, M., Giardino, C., 2021a. Hyperspectral retrievals of phytoplankton absorption and chlorophyll-a in inland and nearshore coastal waters. Remote Sens. Environ. 253, 112200. https://doi.org/10.1016/j.rse.2020.112200.
Pahlevan, N., Mangin, A., Balasubramanian, S.V., Smith, B., Alikas, K., Arai, K., Barbosa, C., Bélanger, S., Binding, C., Bresciani, M., Giardino, C., Gurlin, D., Fan, Y., Harmel, T., Hunter, P., Ishikaza, J., Kratzer, S., Lehmann, M.K., Ligi, M., Ma, R., Martin-Lauzer, F.-R., Olmanson, L., Oppelt, N., Pan, Y., Peters, S., Reynaud, N., Sander de Carvalho, L.A., Simis, S., Spyrakos, E., Steinmetz, F., Stelzer, K., Sterckx, S., Tormos, T., Tyler, A., Vanhellemont, Q., Warren, M., 2021b. ACIX-Aqua: A global assessment of atmospheric correction methods for Landsat-8 and Sentinel-2 over lakes, rivers, and coastal waters. Remote Sens. Environ. 258, 112366.
Pearlman, J.S., Barry, P.S., Segal, C.C., Shepanski, J., Beiso, D., Carman, S.L., 2003. Hyperion, a space-based imaging spectrometer. IEEE Trans. Geosci. Remote Sens. 41 (6), 1160–1173. https://doi.org/10.1109/TGRS.2003.815018.
Pengra, B.W., Johnston, C.A., Loveland, T.R., 2007. Mapping an invasive plant, Phragmites australis, in coastal wetlands using the EO-1 Hyperion hyperspectral sensor. Remote Sens. Environ. 108 (1), 74–81. https://doi.org/10.1016/j.rse.2006.11.002.
Peters, S., Laanen, M., Groetsch, P., Ghezehegn, S., Poser, K., Hommersom, A., De Reus, E., Spaias, L., 2018. WISPstation: A new autonomous above water radiometer system. In: Proceedings of the Ocean Optics XXIV Conference, Dubrovnik, Croatia, pp. 7–12.
Pignatti, S., Cavalli, R.M., Cuomo, V., Fusilli, L., Pascucci, S., Poscolieri, M., Santini, F., 2009. Evaluating Hyperion capability for land cover mapping in a fragmented ecosystem: Pollino National Park. Italy. Remote Sens. Environ. 113 (3), 622–634. https://doi.org/10.1016/j.rse.2008.11.006.
Pignatti, S., Amodeo, A., Carfora, M.F., Casa, R., Mona, L., Palombo, A., Pascucci, S., Rosoldi, M., Santini, F., Laneve, G., 2022. PRISMA L1 and L2 Performances within the PRISCAV Project: The Pignola Test Site in Southern Italy. Remote Sens. 14 (9), 1985.
Rast, M., Painter, T.H., 2019. Earth observation imaging spectroscopy for terrestrial systems: An overview of its history, techniques, and applications of its missions. Surv. Geophys. 40 (3), 303–331. https://doi.org/10.1007/s10712-019-09517-z.
Ruddick, K.G., De Cauwer, V., Park, Y.J., Moore, G., 2006. Seaborne measurements of near infrared water-leaving reflectance: The similarity spectrum for turbid waters. Limnol. Oceanogr. 51 (2), 1167–1179.
Ruddick, K.G., Voss, K., Boss, E., Castagna, A., Frouin, R., Gilerson, A., Hieronymi, M., Johnsonn, B.C., Kuusk, J., Lee, Z., et al., 2019. A review of protocols for fiducial reference measurements of water-leaving radiance for validation of satellite remote-sensing data over water. Remote Sens. 11 (19), 2198. https://doi.org/10.3390/rs11192198.
Santini, F., Alberotanza, L., Cavalli, R.M., Pignatti, S., 2010. A two-step optimization procedure for assessing water constituent concentrations by hyperspectral remote sensing techniques: an application to the highly turbid Venice lagoon waters.

Remote Sens. Environ. 114 (4), 887–898. https://doi.org/10.1016/j.rse.2009.12.001.
Schaepman, M.E., Ustin, S.L., Plaza, A.J., Painter, T.H., Verrelst, J., Liang, S., 2009. Earth system science related imaging spectroscopy—An assessment. Remote Sens. Environ. 113, S123–S137. https://doi.org/10.1016/j.rse.2009.03.001.
Schott, J.R., 2007. Remote sensing: the image chain approach. 2nd ed., Oxford University Press, New York.
Simis, S.G., Olsson, J., 2013. Unattended processing of shipborne hyperspectral reflectance measurements. Remote Sens. Environ. 135, 202–212.
Soppa, M.A., Silva, B., Steinmetz, F., Keith, D., Scheffler, D., Bohn, N., Bracher, A., 2021. Assessment of Polymer atmospheric correction algorithm for hyperspectral remote sensing imagery over coastal waters. Sensors 21 (12), 4125. https://doi.org/10.3390/s21124125.
Sterckx, S., Brown, I., Kääb, A., Krol, M., Morrow, R., Veefkind, P., Boersma, K.F., De Mazière, M., Fox, N., Thorne, P., 2020. Towards a European Cal/Val service for earth observation. Int. J. Remote Sens. 41 (12), 4496–4511. https://doi.org/10.1080/01431161.2020.1718240.
Tagliabue, G., Boschetti, M., Bramati, G., Candiani, G., Colombo, R., Nutini, F., Pompilio, L., Rivera-Caicedo, J.P., Rossi, M., Rossini, M., Verrelst, J., Panigada, C., 2022. Hybrid retrieval of crop traits from multi-temporal PRISMA hyperspectral imagery. ISPRS J. Photogramm. Remote Sens. 187, 362–377.
Taramelli, A., Tornato, A., Magliozzi, M.L., Mariani, S., Valentini, E., Zavagli, M., Costantini, M., Nieke, J., Adams, J., Rast, M., 2020. An interaction methodology to collect and assess user-driven requirements to define potential opportunities of future hyperspectral imaging sentinel mission. Remote Sens. 12 (8), 1286. https://doi.org/10.3390/rs12081286.
Thompson, D.R., Guanter, L., Berk, A., Gao, B.C., Richter, R., Schläpfer, D., Thome, K.J., 2019. Retrieval of atmospheric parameters and surface reflectance from visible and shortwave infrared imaging spectroscopy data. Surv. Geophys. 40 (3), 333–360. https://doi.org/10.1007/s10712-018-9488-9.
Thuillier, G., Hersé, M., Foujols, T., Peetermans, W., Gillotay, D., Simon, P.C., Mandel, H., 2003. The solar spectral irradiance from 200 to 2400 nm as measured by the SOLSPEC spectrometer from the ATLAS and EURECA missions. Sol. Phys. 214 (1), 1–22. https://doi.org/10.1023/A:1024048429145.
Tilstone, G.H., Pardo, S., Simis, S.G., Qin, P., Selmes, N., Dessailly, D., Kwiatkowska, E., 2021. Consistency between Satellite Ocean Colour Products under High Coloured Dissolved Organic Matter Absorption in the Baltic Sea. Remote Sens. 14 (1), 89. https://doi.org/10.3390/rs14010089.
Transon, J., d'Andrimont, R., Maugnard, A., Defourny, P., 2018. Survey of hyperspectral earth observation applications from space in the sentinel-2 context. Remote Sens. 10 (2), 157. https://doi.org/10.3390/rs10020157.
Valente, A., Sathyendranath, S., Brotas, V., Groom, S., Grant, M., Taberner, M., Antoine, D., Arnone, R., Balch, Barker, K., et al., 2019. A compilation of global bio-optical in situ data for ocean-colour satellite applications–version two. Earth Syst. Sci. Data 11 (3), 1037–1068.
Vanhellemont, Q., 2019. Adaptation of the dark spectrum fitting atmospheric correction for aquatic applications of the Landsat and Sentinel-2 archives. Remote Sens. Environ. 225, 175–192. https://doi.org/10.1016/j.rse.2019.03.010.
Vanhellemont, Q., 2020. Sensitivity analysis of the dark spectrum fitting atmospheric correction for metre-and decametre-scale satellite imagery using autonomous hyperspectral radiometry. Opt. Express 28 (20), 29948–29965. https://doi.org/10.1364/OE.397456.
Vanhellemont, Q., Ruddick, K., 2018. Atmospheric correction of metre-scale optical satellite data for inland and coastal water applications. Remote Sens. Environ. 216, 586–597. https://doi.org/10.1016/j.rse.2018.07.015.
Vanhellemont, Q., Ruddick, K., 2021. Atmospheric correction of Sentinel-3/OLCI data for mapping of suspended particulate matter and chlorophyll-a concentration in Belgian turbid coastal waters. Remote Sens. Environ. 256, 112284. https://doi.org/10.1016/j.rse.2021.112284.
Vansteenwegen, D., Ruddick, K., Cattrijsse, A., Vanhellemont, Q., Beck, M., 2019. The pan-and-tilt hyperspectral radiometer system (PANTHYR) for autonomous satellite validation measurements - Prototype design and testing. Remote Sens. 11 (11), 1360.
Vermote, E.F., El Saleous, N., Justice, C.O., Kaufman, Y.J., Privette, J.L., Remer, L., Roger, J.C., Tanre, D., 1997. Atmospheric correction of visible to middle-infrared EOS-MODIS data over land surfaces: Background, operational algorithm and validation. J. Geophys. Res. Atmos. 102 (D14), 17131–17141. https://doi.org/10.1029/97JD00201.
Warren, M.A., Simis, S.G., Martinez-Vicente, V., Poser, K., Bresciani, M., Alikas, K., Spyrakos, E., Giardino, C., Ansper, A., 2019. Assessment of atmospheric correction algorithms for the Sentinel-2A MultiSpectral Imager over coastal and inland waters. Remote Sens. Environ. 225, 267–289. https://doi.org/10.1016/j.rse.2019.03.018.
Werdell, P.J., Behrenfeld, M.J., Bontempi, P.S., Boss, E., Cairns, B., Davis, G.T., Franz, B. A., Gliese, U.B., Gorman, E.T., Hasekamp, O., Knobelspiesse, K.D., Mannino, A., Martins, J.V., McClain, C.R., Meister, G., Remer, L.A., 2019. The Plankton, Aerosol, Cloud, ocean Ecosystem mission: status, science, advances. Bull. Amer. Meteor. 100 (9), 1775–1794.
Wettle, M., Brando, V.E., Dekker, A.G., 2004. A methodology for retrieval of environmental noise equivalent spectra applied to four Hyperion scenes of the same tropical coral reef. Remote Sens. Environ. 93 (1–2), 188–197.
Zibordi, G., Berthon, J.F., Bulgarelli, B., D'alimonte, D., Linde, D.V.D., Mélin, F., Targa, C., 2004a. Ocean colour validation activities at the Acqua Alta Oceanographic Tower in the northern Adriatic Sea. Int. J. Remote Sens. 25 (7–8), 1533–1537. https://doi.org/10.1080/01431160310001592553.
Zibordi, G., Mélin, F., Hooker, S.B., D'Alimonte, D., Holben, B., 2004b. An autonomous above-water system for the validation of ocean color radiance data. IEEE Trans. Geosci. Remote Sens. 42 (2), 401–415. https://doi.org/10.1109/TGRS.2003.821064.
Zibordi, G., Mélin, F., Berthon, J.F., 2006. Comparison of SeaWiFS, MODIS and MERIS radiometric products at a coastal site. Geophys. Res. Lett. 33 (6).
Zibordi, G., Mélin, F., Berthon, J.-F., Holben, B., Slutsker, I., Giles, D., D'Alimonte, D., Vandemark, D., Feng, H., Schuster, G., Fabbri, B.E., Kaitala, S., Seppälä, J., 2009a. AERONET-OC: a network for the validation of ocean color primary products. J. Atmos. Ocean. Technol. 26 (8), 1634–1651.
Zibordi, G., Berthon, J.F., Mélin, F., D'Alimonte, D., Kaitala, S., 2009b. Validation of satellite ocean color primary products at optically complex coastal sites: Northern Adriatic Sea, Northern Baltic Proper and Gulf of Finland. Remote Sens. Environ. 113 (12), 2574–2591. https://doi.org/10.1016/j.rse.2009.07.013.
Zibordi, G., Ruddick, K., Ansko, I., Moore, G., Kratzer, S., Icely, J., Reinart, A., 2012. In situ determination of the remote sensing reflectance: an inter-comparison. Ocean Sci. 8 (4), 567–586. https://doi.org/10.5194/os-8-567-2012.
Zibordi, G., Holben, B.N., Talone, M., D'Alimonte, D., Slutsker, I., Giles, D.M., Sorokin, M.G., 2020. Advances in the ocean color component of the Aerosol Robotic Network (AERONET-OC). J. Atmos. Ocean. Technol. 38 (4), 725–746.
Zibordi, G., Kwiatkowska, E., Mélin, F., Talone, M., Cazzaniga, I., Dessailly, D., Gossn, J. I., 2022. Assessment of OLCI-A and OLCI-B radiometric data products across European seas. Remote Sens. Environ. 272, 112911 https://doi.org/10.1016/j.rse.2022.112911.